

1
2 **Dynamic and thermodynamic contribution to the October 2019 exceptional**
3 **rainfall in West Central Africa**
4

5 **Kevin Kenfack^{1*} · Francesco Marra³ · Zéphirin Yepdo Djomou^{1,2} · Lucie Angennes Djiotang**
6 **Tchotchou¹ · Alain Tchio Tamoffo⁴ · Derbetini Appolinaire Vondou¹**
7

8 ¹Laboratory for Environmental Modelling and Atmospheric Physics (LEMAP), Physics Department,
9 University of Yaoundé 1, Yaoundé, Cameroon

10 ²National Institute of Cartography, Cameroon

11 ³Department of Geosciences, University of Padova, Italy

12 ⁴Climate Service Center Germany (GERICS), Helmholtz-Zentrum Hereon, Fischertwiete 1, 20095
13 Hamburg, Germany

14
15
16 Corresponding author: **Kevin Kenfack**

17 Email: **kevinkenfack46@gmail.com**

18 ORCID: **0000-0003-1694-4906**

19 Kevin Kenfack's ORCID: 0000-0003-1694-4906

20 Francesco Marra's ORCID: 0000-0003-0573-9202

21 Lucie Angennes Djiotang Tchotchou's ORCID: 0000-0003-2860-428X

22 Alain Tchio Tamoffo's ORCID: 0000-0001-8482-8881

23 Derbetini Appolinaire Vondou's ORCID: 0000-0002-8681-5328
24
25
26
27
28
29

30 **Abstract**

31 Exceptional rainfall hit West Central Africa in October 2019. To understand the underlying
32 mechanisms, we examined the regional moisture and Moist Static Energy (MSE) budgets intending
33 to highlight the importance of the dynamic and thermodynamic effects associated with this historic
34 event. Analysis of the moisture budget reveals that the precipitation anomalies in October were
35 mainly controlled by dynamic effects. Horizontal moisture advection induced by horizontal wind
36 anomalies controls extreme precipitation north of West Central Africa, while vertical moisture
37 advection induced by vertical velocity anomalies controls extreme precipitation south of West
38 Central Africa. Changes in the thermodynamic effect, although not the key factor responsible for the
39 events of October 2019, contribute up to 35% of the total effect on the northern part and 15% on the
40 southern part of the domain. The residual term on the northern part is important and provides a caveat
41 when estimating dynamic and thermodynamic processes. Diagnosis of the MSE balance averaged
42 over the northern part of west Central Africa shows that the anomalous vertical motion is dominated
43 by the dynamic effect, i.e. the wet enthalpy advection induced by the horizontal wind anomalies. This
44 is confirmed by the high spatial correlation ($r = 0.6$) between the two terms compared to the other
45 terms. Whereas to the west of the Congo Basin, the increase in the net energy balance dominated the
46 changes in vertical motion ($r = 0.51$). The horizontal advection of the MSE induced by the anomalies
47 of the wet enthalpy and the vertical advection of the MSE induced by the anomalies of the MSE seem
48 less important ($r = 0.29$ and -0.19 to the north and -0.17 and 0.03 to the south respectively). The
49 strong anomalies in the MSE balance in the north are linked to its meridional component, in
50 particular the meridional wind anomalies in the dynamic effect and the meridional anomalies in latent
51 heat in the thermodynamic effect. Our results suggest that dynamic and thermodynamic effects
52 should be jointly considered for adequately anticipating this kind of extreme event. Understanding
53 the associated mechanisms could help us improve our forecasts and projections, and increase the
54 region's population resilience to these extreme weather events.

55 **Keywords:** West Central Africa · Moisture budget · Moist static energy budget · Precipitation · wet
56 enthalpy

57

58

59

60

62 **1 Introduction**

63 Equatorial Africa recorded unprecedented amounts of rainfall in October and November 2019
64 (Wainwright et al, 2020). Such a significant amount of precipitation is not without consequences for
65 the population and the environment. In October, in most parts of East Africa in general, and in Kenya
66 in particular, extreme rainfall led to flooding and landslides, provoking major destruction, with more
67 than 100 deaths and around 18,000 people displaced internally and to neighbouring countries
68 (<http://floodlist.com/africa/kenya-floods-november-2019>). In Central Africa, the Democratic
69 Republic of Congo has been devastated by major flooding and forestry disruption along the Congo
70 River, forcing many people to move (Gou et al. 2022). In the Central African Republic, extreme and
71 persistent rainfall caused significant flooding and landslides, including the Oubangui River
72 overflowing nearly 60 km of its coastline (Igri et al. 2023). In addition, the night of 27 to 28 October
73 2019 was disastrous in the West Cameroon region, mainly in the locality of Bafoussam where
74 extreme rainfall for about 36 hours caused a landslide, resulting in significant material damage with
75 45 dead and others missing (Aretouyap et al. 2021; Mfondoum et al. 2021; Wantim et al. 2023). The
76 episode was associated with a thermal depression over the Sahara and with anomalously high Sea
77 Surface Temperatures (SST). The occurrence of these conditions may change in response to
78 anthropogenic global warming, raising the question of whether devastating events such as the one of
79 October 2019 could occur more frequently in the future (Nicholson et al. 2022). In particular, given
80 that climate models predict an increasing trend in extreme rainfall in the region (Fotso-Nguemo et al.
81 2018, 2019; Sonkoué et al. 2018; Tamoffo et al. 2019, 2023) and that extreme precipitation in the
82 region is associated with vegetation dynamics (Zhou et al. 2014; Mariotti et al. 2014; Marra et al.
83 2022; Garcin et al. 2018), it is crucial to understand the thermodynamic and dynamic mechanisms
84 underlying these exceptional events of October 2019.

85 Recent studies have attempted to investigate the causes of extreme rainfall during the exceptional
86 period of October 2019 in Equatorial Africa. Nicholson et al. (2022) showed that the heavy rainfall
87 on the Guinean coast was reinforced by positive sea surface temperature anomalies along the Atlantic
88 coast. This process leads to a significant advection of the moisture flux from the Atlantic, combined
89 with the convergence of the moisture, which contributed to the increase in rainfall in the region
90 (Pokam et al. 2011, Kuete et al. 2019). Wainwright et al. (2020) pointed out that the increase in
91 rainfall over East Africa was a consequence of the positive phase of the Indian Ocean Dipole. Indeed,
92 Black et al. (2005) reported that during periods of the year when the dipole mode index (DMI) IOD
93 events are greater than 0.5°C over a period of 3 consecutive months and when the zonal SST gradient

94 is reversed over several months, the resulting increase in rainfall over East Africa is important. In
95 addition, the positive IOD event of 2019 lasted from late summer through to December, influencing
96 rainfall over East Africa.

97 Rainfall variability in Central Africa is highly dependent on the convergence of atmospheric
98 moisture (Pokam et al. 2012; Washington et al., 2013; Dyer et al., 2017; Hua et al., 2019; Taguela et
99 al. 2022; Tamoffo et al. 2023b,2024). Under the effect of global warming, the increase in extreme
100 precipitation is a consequence of the increase in available atmospheric humidity (Nicholson et al
101 2022). Although previous studies have focused on analyzing meteorological factors, there is still a
102 general lack of knowledge about quantifying the dynamic and thermodynamic effects associated with
103 these extremes of precipitation. In recent years, the decomposition of the water balance behind
104 precipitation anomalies is often used to isolate the dynamic and thermodynamic contributions to
105 extreme events (Li et al., 2017; Oueslati et al., 2019; Wen et al., 2022; Kenfack et al., 2023,2024).
106 Water balance analysis has proved to be a useful tool for understanding anomaly fields in mean
107 precipitation under the influence of global warming (Seager et al. 2014). Moist static energy (MSE),
108 in particular, is a useful parameter for investigating the contribution of atmospheric moisture and
109 analysing vertical velocity (Wang and Li, 2020a, 2020b; Bell et a. 2015; Neelin, 2021; Nana et al.
110 2023; Andrews et al. 2023; Longandjo and Raoul, 2024; Kenfack et al. 2024). Recently, Kenfack et
111 al. (2024) showed that, in the Congo Basin, the structure of the horizontal moisture advection
112 anomalies is similar to that of the MSE advection anomalies during rainy seasons March-April-May
113 (MAM) and September-October-November (SON). In addition, the atmospheric heating source has
114 been identified as an indicator of precipitation (He et al. 2021). The increase in diabatic heating on
115 the coast can contribute to the acceleration of near-surface winds (Pokam et al. 2014). An increase in
116 this quantity implies an increase in latent warming, associated with a strong ocean-continent
117 horizontal moisture gradient, which can lead to a strengthening of the boundary layer MSE, with a
118 positive feedback process leading to extreme precipitation. Further, it has been demonstrated that a
119 simultaneous reduction in the heating source and rainfall has been observed in reanalyses over recent
120 decades in the Congo Basin (Kenfack et al. 2024). Given the highlighted importance of moisture,
121 MSE and heating sources on rainfall variability, we adopt in this study an approach based on diabatic
122 heating, water balance and MSE to diagnose dynamic and thermodynamic processes associated with
123 the October 2019 rainfall extremes over West Equatorial Africa.

124 The remainder of the paper is structured as follows. A description of the observation and
125 reanalysis data, and analysis methods is presented in Section 2. Section 3 describes the diabatic
126 heating source and the performance of the reanalysis in capturing the October 2019 precipitation
127 extremes. In Section 4, we investigate the dynamic and thermodynamic effects associated with the

128 moisture balance. The analysis of the dynamic and thermodynamic effects associated with the MSE
129 budget during the October 2019 rainfall anomaly period over West Central Africa is presented in
130 Section 5. Section 6 is conclusions and discussions.

131

132 **2 Data and methods**

133 **2.1. Data**

134 In this study, datasets from the fifth version of the European Centre for Medium-Range Weather
135 Forecasts reanalysis, known as ERA5 (Hersbach et al., 2020), are used for the analyses. Johannsen
136 et al. (2019) established that over equatorial Africa, ERA5 significantly improves over ERA-
137 Interim (which represents the previous dataset), particularly in the description of the hydrological
138 cycle. In addition, Cook and Vizy (2021) have shown that ERA5 represents well the spatial
139 distribution of precipitation and atmospheric dynamic fields compared with previous generations,
140 particularly over the Congo Basin. With a spatial resolution of $0.25^{\circ} \times 0.25^{\circ}$, ERA5 is a global
141 reanalysis dataset available from 1979 to the present, covering 137 pressure levels from the surface
142 to 0.01 hPa. Monthly variables including horizontal and vertical wind components, geopotential,
143 evaporation, humidity, heat flux and temperature are used in this study. For all variables, anomalies
144 are obtained by removing the 30-year mean of the period 1988 to 2017. In order to reinforce the
145 robustness of the results, several variables, such as winds (horizontal and vertical), specific
146 humidity, precipitation and evaporation, obtained from the Modern-Era Retrospective Analysis for
147 Research and Applications, version 2 (MERRA2), which provides data from 1980 to the present
148 day (Gelaro et al., 2017), were used in this study. To assess ERA5's ability to detect October 2019
149 precipitation extremes, we used three observational datasets, including rain gauge products and
150 gauge-adjusted satellite products: the Climate Hazards Group InfraRed Precipitation with Stations
151 (CHIRPS) gridded dataset, available at a resolution of $0.05^{\circ} \times 0.05^{\circ}$ (Funk et al., 2015); the Global
152 Precipitation Climatology Project (GPCP-v2.2) with a grid spacing of $2.5^{\circ} \times 2.5^{\circ}$ (Huffman et al.,
153 2009); the Climatic Research Unit (CRU-TS4.03) gridded data at a resolution of $0.5^{\circ} \times 0.5^{\circ}$ (Harris
154 et al., 2020).

155

156 **2.2 Methods**

157 **2.2.1 Diabatic heating**

158 Apparent diabatic heating as proposed by Yanai and Tomita (1998) and Pokam et al. (2014) is
159 defined as follows:

$$160 \quad Q = \chi \left(\frac{\partial \theta}{\partial t} + u \frac{\partial \theta}{\partial x} + v \frac{\partial \theta}{\partial y} + \omega \frac{\partial \theta}{\partial p} \right) \quad (1)$$

$$161 \quad \chi = c_p \left(\frac{T}{\theta} \right) \quad (2)$$

162 In equations 1 and 2, C_p (1,005 J Kg⁻¹ K⁻¹) denotes the specific heat at constant pressure, θ is the
 163 potential temperature, ω is the vertical velocity (hPa s⁻¹), and $V=(u, v)$ is the vector of horizontal
 164 velocities. T (K) and p (hPa) represent the air temperature and the barometric pressure, respectively.

165 To quantify the monthly mean heating rate τ (K day⁻¹) related to apparent heating, we use the
 166 relation:

$$167 \quad \tau = \frac{Q}{c_p} \quad (3)$$

168 where Q is the combination of heat from radiation, latent heat from condensation and the
 169 convergence of vertical vortical transport of sensible heat.

170

171 2.2.2 Diagnosis of the moisture budget

172 The moisture budget used to quantify the contributions of evaporation and the horizontal and
 173 vertical components associated with the circulation of moist air in the atmosphere (Seager et al.,
 174 2010; Oueslati et al., 2019; Jiang et al., 2020; Moon and Ha, 2020; Wen et al., 2022; Zhao et al.,
 175 2022; Sheng et al., 2023; Kenfack et al., 2024) is defined as follows:

$$176 \quad \langle \partial_t q \rangle + \langle V \cdot \nabla_h q \rangle + \langle \omega \cdot \partial_p q \rangle = E - P \quad (4)$$

177 In Eq. 4, q represents the specific humidity, $V=(u,v)$ denotes the horizontal wind and ω the vertical
 178 pressure velocity. E denotes surface evaporation and P precipitation. Angle brackets " $\langle \rangle$ "
 179 signify the mass integral from the surface ($p_s = 1000$ hPa) to a pressure $p_t = 300$ hPa,
 180 which represents the top of the atmosphere layer considered. The first term on the left of equation 4
 181 can be neglected given its small variation over time on a monthly scale and could contribute to the
 182 residuals (Wen et al. 2022; Sheng et al. 2023). To estimate the horizontal and vertical moisture
 183 advection components, we decompose equation 4 into its different linear and residual terms as
 184 follows:

$$185 \quad P' = E' - \langle \nabla \cdot \nabla q' \rangle - \langle V' \cdot \nabla \bar{q} \rangle - \langle \bar{\omega} \partial_p q' \rangle - \langle \omega' \partial_p \bar{q} \rangle + Res \quad (5)$$

186 In Eq. 5, the overbar indicates the monthly mean climatology from 1988 to 2017 and primes
 187 indicate deviations from this climatology; The residual term "Res" contains the non-linear and
 188 transient processes associated with the joint variations in water vapor content and circulation. The
 189 terms $\langle -V' \cdot \nabla \bar{q} \rangle$ and $\langle -\omega' \partial_p \bar{q} \rangle$ represent the dynamic contributions (or effect) and refer to

190 the moisture advection induced by the horizontal wind and by the vertical pressure velocity,
 191 respectively. The terms $\langle -\nabla \cdot \nabla q' \rangle$ and $\langle -\bar{\omega} \partial_p q' \rangle$ represent the thermodynamic contributions
 192 (or effect), and refer to the contribution of water vapor.

193

194 2.2.3 Diagnosis of the MSE budget

195 The MSE equation is defined as follows:

$$196 \quad \langle \partial_t (c_v T + L_v q) \rangle + \langle \mathbf{V} \cdot \nabla M \rangle + \langle \bar{\omega} \partial_p m \rangle = F_{net} \quad (6)$$

197 where the moist enthalpy is

$$198 \quad M = c_p T + L_v q \quad (7)$$

199 and the MSE is

$$200 \quad m = c_p T + L_v q + \Psi \quad (8)$$

201 In equations 7 and 8, c_p (c_v) represents the specific heat at constant pressure (the specific heat at
 202 constant volume); T is the air temperature and Ψ the geopotential. F_{net} is the net energy entering
 203 the atmospheric column at the surface and top of the atmosphere (latent heat, sum of sensible heat,
 204 and shortwave and longwave radiative fluxes). Similar to the moisture flux equation, the first term on
 205 the left of equation 6 can be neglected given its small variation over time on a monthly scale and
 206 contributes to the residuals. In addition, it should be noted that variations in geopotential height
 207 along pressure levels are neglected in this formulation of the MSE budget. The remaining terms in
 208 equation 6 can be decomposed into horizontal and vertical advection components, as described by:

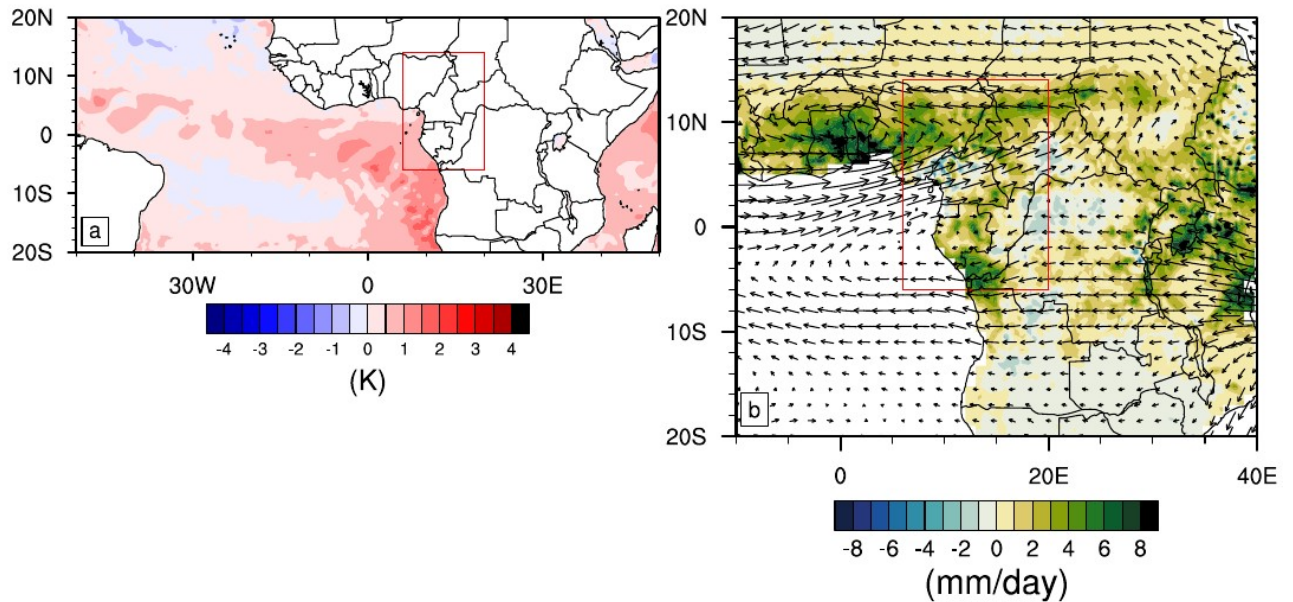
$$209 \quad \langle \omega' \partial_p \bar{m} \rangle = -\langle \nabla \cdot \nabla M' \rangle - \langle \mathbf{V}' \cdot \nabla M \rangle - \langle \bar{\omega} \partial_p m' \rangle + F'_{net} + Res \quad (9)$$

210 Anomalous vertical motion is analysed using this equation with a given profile of \bar{m} . Similar to the
 211 convention adopted for decomposing the moisture flux, the term $-\langle \mathbf{V}' \cdot \nabla M \rangle$ relates to the
 212 anomalous MSE associated with the atmospheric circulation and contains the dynamic contribution
 213 (or effect), while the two terms $-\langle \nabla \cdot \nabla M' \rangle$ and $-\langle \bar{\omega} \partial_p m' \rangle$ refer to the thermodynamic
 214 contribution (or effect), which is crucial for diagnosing the thermal state of the atmosphere
 215 associated with the increase in the vertical rise of the air.

216

217 3 Diabatic heating and extreme rainfall

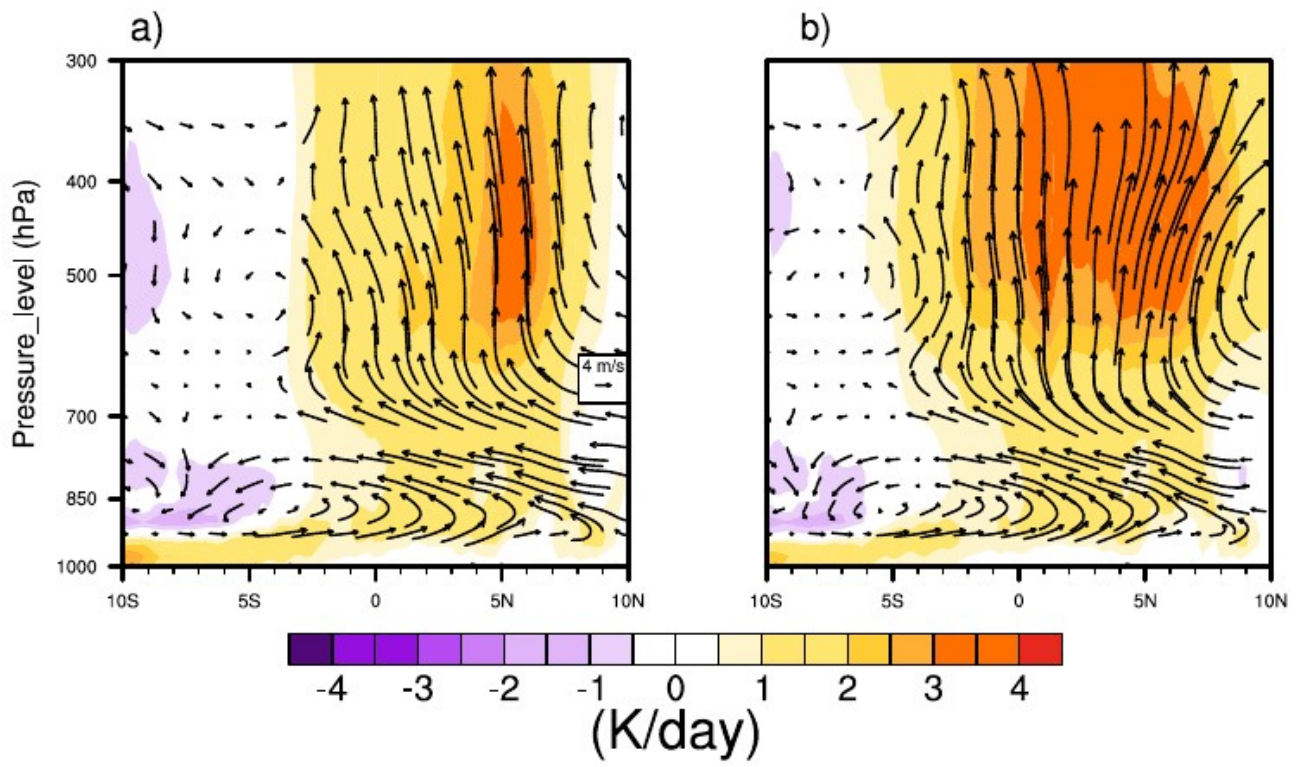
218 The increase in SSTs in the eastern Atlantic (Fig. 1a) has been identified as one of the causes of the
219 positive precipitation anomalies over western central Africa in October 2019. The warming contrast
220 between the ocean and the continent favoured the strengthening of the moisture advection
221 associated with the precipitation anomalies over West Central Africa (Fig. 1b). This is in agreement
222 with Nicholson et al. (2022).



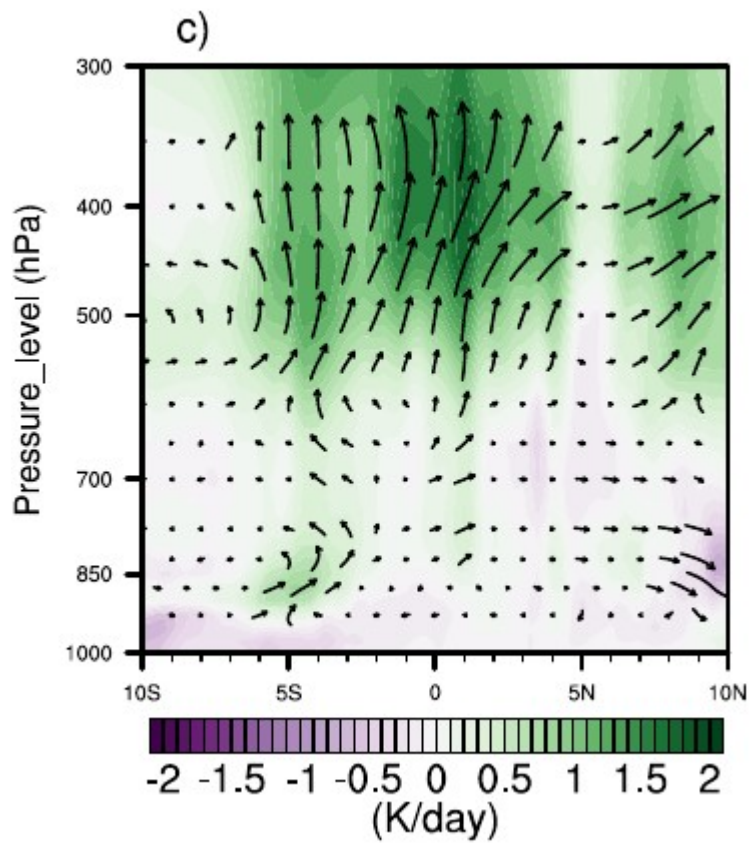
223

224 **Fig 1.** SST a) and rainfall b) anomalies during October 2019. The vectors represent anomalies of
225 vertically integrated atmospheric moisture flux. The red box indicates the Central West Africa area.

226 Figure 2 represents the mean vertical profile (pressure-latitude) of diabatic heating averaged
227 between 6° and 20°E during SON for the 1988-2017 climatology (Fig. 2a) and the corresponding
228 profile for 2019 (Fig. 2b). During SON, the main source of heat is located between 3°S and 9°N for
229 climatology, and between 5°S and 13°N for 2019.



230



231

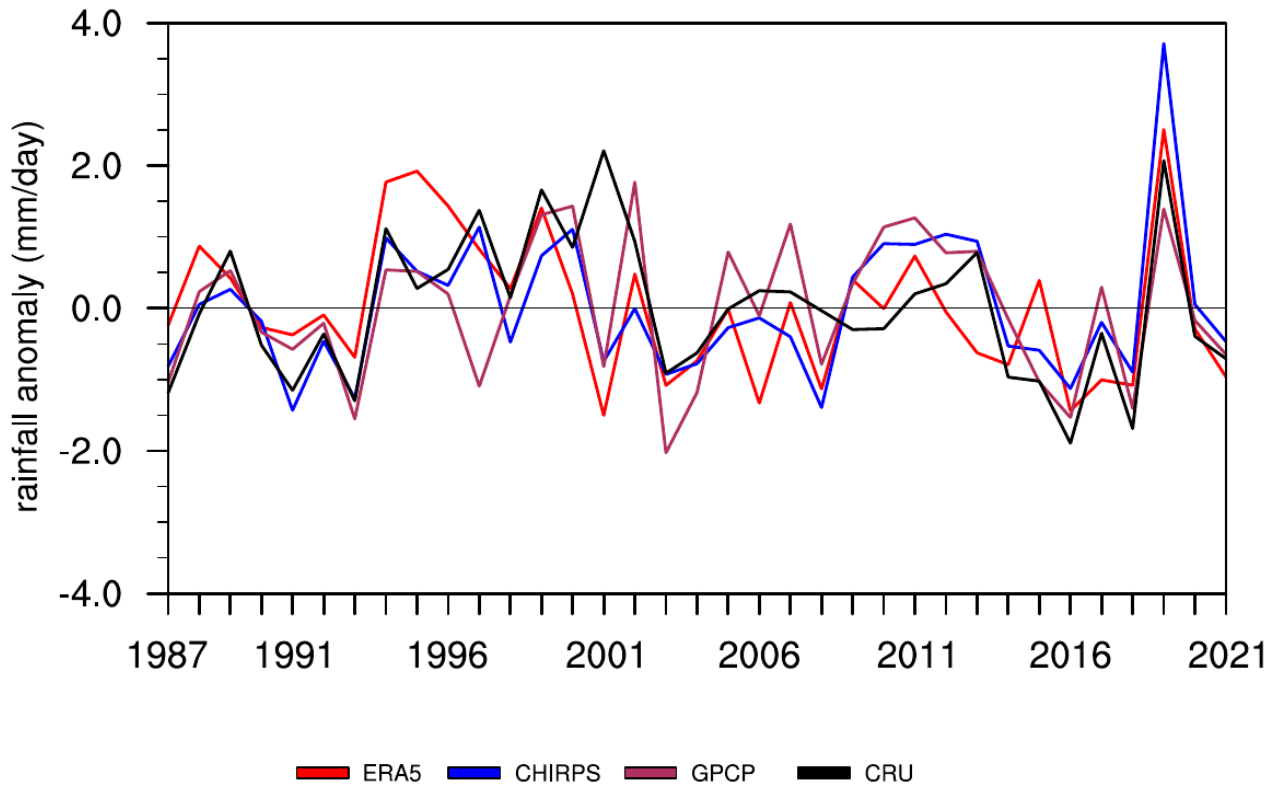
232 **Fig 2.** Diabatic heating and divergent meridional circulation (vectors; ms^{-1}) during the SON
 233 season for a) 1988-2017 avg, b) 2019 avg and c) the anomaly, all averaged between the 6° and

234 20°E. As the vertical velocity is much weaker than the meridional wind, its values have been
235 enhanced by a factor of 600 for the clarity of the graph.

236

237 However, 2019 presents a more extensive and pronounced source of heat compared with the
238 climatology 1988-2017. A 3-4 $K day^{-1}$ heating, more intense in 2019, occurred from 600 hPa. A
239 cooling of 1- 2 $K day^{-1}$ took place around 850 hPa in the south and from 550 hPa in the north. The
240 profound heating observed from 600 hPa originates at the surface on the southern portion of the
241 domain (10°S). It is reinforced by the contrast between the large positive values and the negative
242 values on either side of the equator between 500 and 400 hPa. The vertical structure of the
243 divergent circulation is also illustrated in Figure 2. The divergent circulation appears more
244 pronounced from 550 hPa in 2019 (Fig. 2b) compared with the climatology of 1988-2017 (Fig. 2a).
245 This is consistent with the warming contrast observed. This uplift was reinforced by the warming of
246 the equatorial Atlantic associated with an abnormally strong thermal low over the Sahara, which led
247 to an acceleration of the dominant meridional flow in the divergent circulation (Fig. 2c). This is in
248 agreement with Nicholson et al. (2022), who highlighted that the West African monsoon was late to
249 withdraw in 2019.

250 Although the SON season has shown significant diabatic heating compared to climatology,
251 October 2019 in particular over West Central Africa recorded extremes of rainfall (Nicholson et al.
252 2022). In this study, we use the ERA5 reanalysis precipitation fields for water balance analysis.
253 This ensures that all the examined physical quantities are consistent across the study. Before doing
254 so, we assessed the performance of ERA5 in detecting the extreme precipitation events in October
255 2019. Figure 3 illustrates the interannual variability of October rainfall anomalies over West Central
256 Africa for the period 1987-2021.



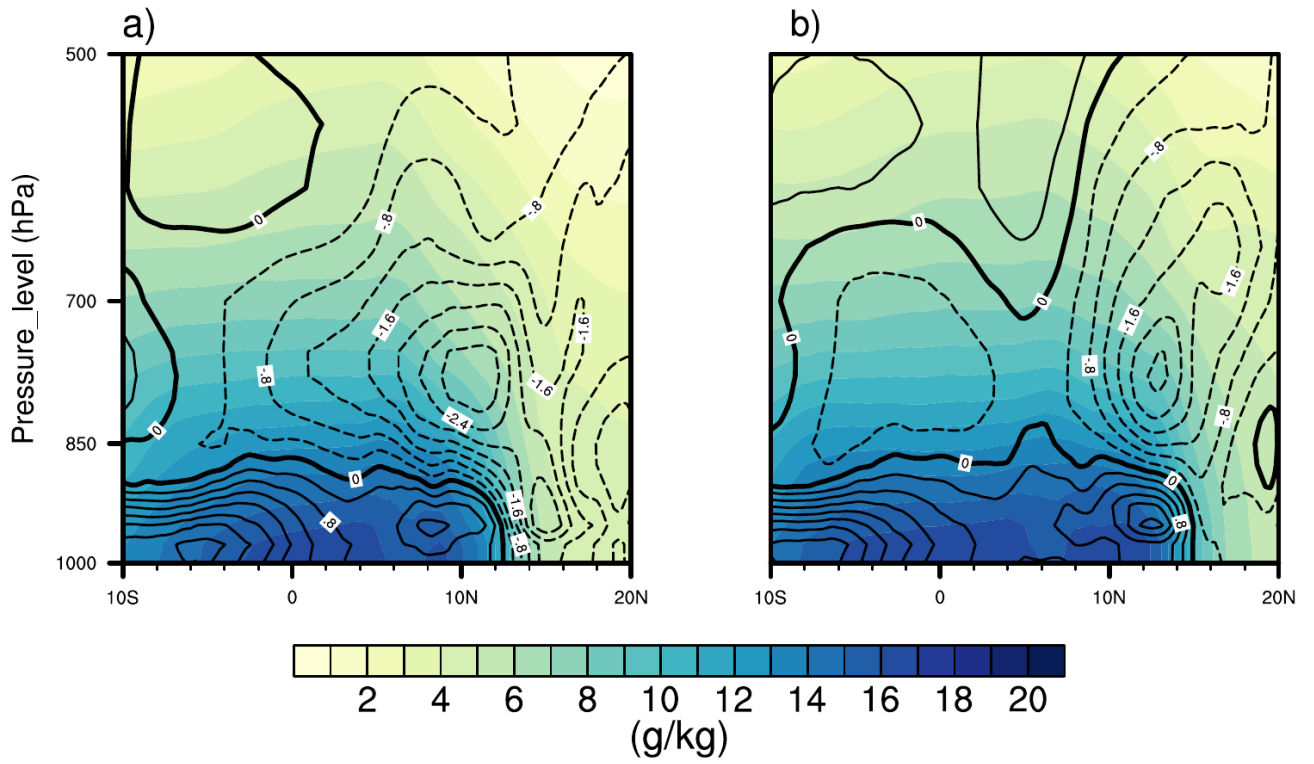
257

258 **Fig 3.** Temporal evolution of October rainfall anomaly over West Central Africa (6°S-14°N, 6°-
 259 20°E), from reanalysis data ERA5 (red) and from observational data CHIRPS (blue), GPCP
 260 (maroon) and CRU (black), covering the period 1987–2021.

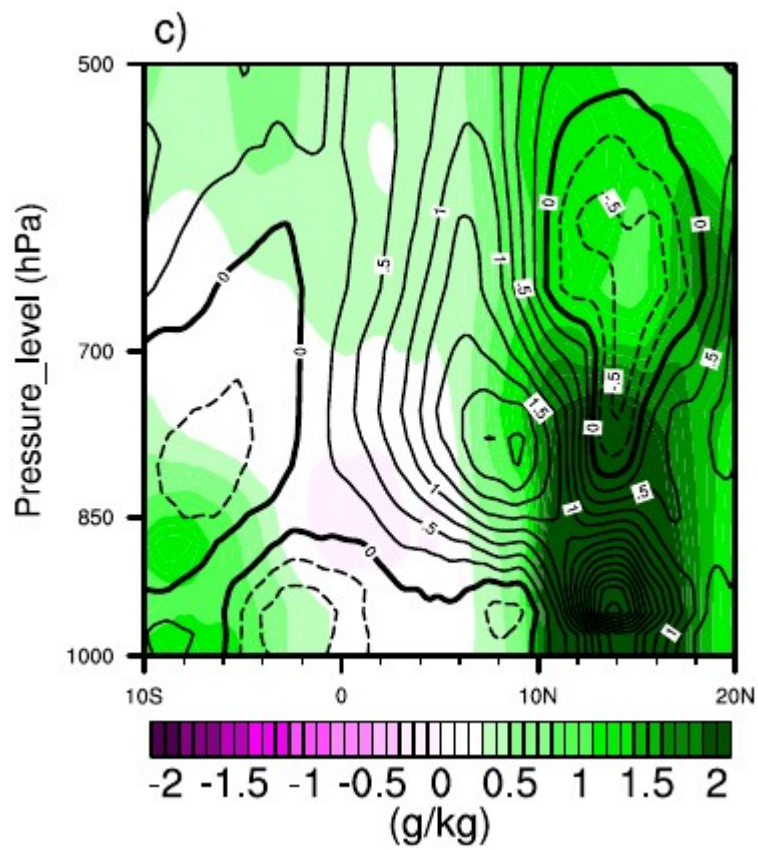
261

262 The ERA5 reanalysis (red) and the CHIRPS (blue), GPCP (maroon) and CRU (black) observations
 263 are consistent in highlighting the high precipitation peak of 2019. CHIRPS shows the highest values
 264 of positive anomalies of up to 3.5 mm day⁻¹, while ERA5 shows values of up to 2.5 mm day⁻¹.
 265 Despite some differences between ERA5 and the observations in representing trends on an
 266 interannual scale (Kenfack et al. 2024), the unprecedented event of October 2019 was well detected.
 267 In addition, the exceptional event is also detected by the MERRA2 reanalysis (Figure S1)

268 The increase in SSTs in the tropical Atlantic reached a record level in October 2019
 269 (Nicholson et al. 2022). This may have resulted in an increased specific humidity over land. Figure
 270 4 depicts the vertical profile (pressure level-latitude) of specific humidity (colors) and meridional
 271 wind (contours) averaged between 6° and 20°E for the 1988-2017 climatology (Fig. 4a), the
 272 October 2019 average (Fig. 4b), and the October 2019 anomaly (Fig. 4c).



273



274

275 **Fig. 4.** Specific humidity and meridional wind (contours: m/s) in October for a) 1988-2017 avg, b)
 276 2019 avg and c) the anomaly, averaged between 6°-20°E.

278 The 1988-2017 climatology is characterized by intense surface specific humidity extending as far as
 279 12°N, whereas the October 2019 average appears to extend further to 15°N. In addition, the
 280 southerly wind in 2019 was more pronounced up to 15°N compared to the climatology. Analysis of
 281 the anomalies confirms that the humidity extended further north in West Central Africa in October
 282 2019, compared with the climatology. The intensification of the southerly wind up to 15°N
 283 indicates that this moisture probably comes from the equatorial Atlantic. This is in agreement with
 284 Kamae et. al (2017), who highlighted that extreme precipitation can be a consequence of changes in
 285 humidity. Indeed, the increase in humidity associated with a substantial heating source contributes
 286 to an increase in precipitation.

287

288 **4 Moisture budget analysis**

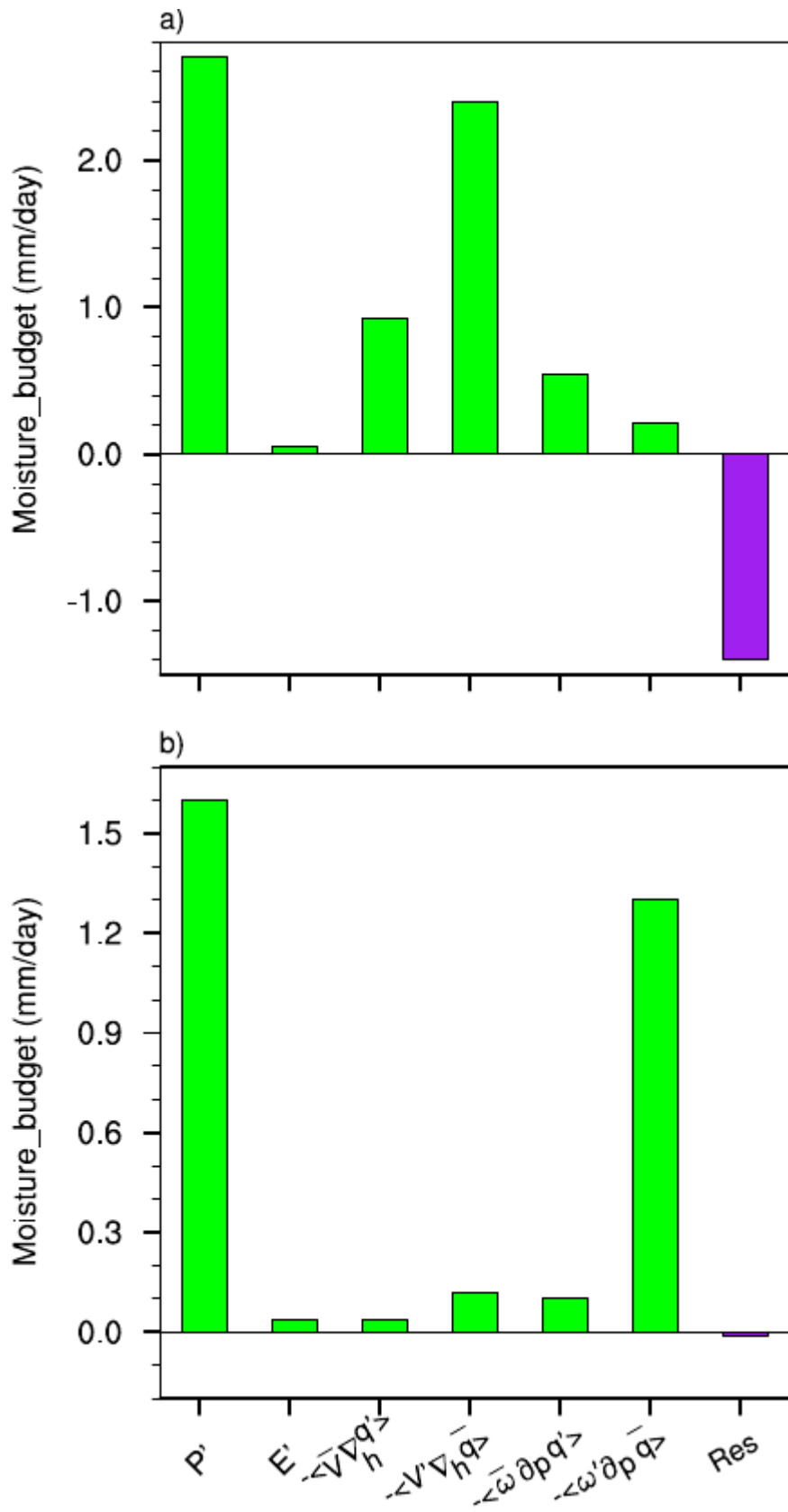
289 Rainfall variability in equatorial Central Africa is strongly dependent on the moisture inputs
 290 associated with atmospheric circulation (Jackson et al., 2009; Cook and Vizu, 2016, 2022; Dyer et
 291 al., 2017; Longandjo and Raoul, 2024). In the Congo Basin, atmospheric heating sources combined
 292 with the vertical advection of moisture induced by anomalous vertical motion are responsible for
 293 most of the interannual variability of precipitation (Kenfack et al., 2024). In this section, we
 294 decompose the moisture budget in equation 5 to examine the processes that led to the October 2019
 295 extreme rainfall over West Central Africa. To do this, we analyse local variations in rainfall
 296 associated with atmospheric moisture introduced into the air column by atmospheric circulation.

297 The monthly anomalies of the different components of the water balance averaged over the
 298 northern part of west-central Africa (6°N-14°N, 6°-20°E) for the month of October 2019 (Fig. 5a)
 299 indicate that the increase in dynamic processes dominated the increase in precipitation. Horizontal
 300 advection of moisture induced by the horizontal wind anomaly $\langle -\mathbf{v}' \cdot \nabla \bar{q} \rangle$ was the most
 301 pronounced component (up to 2.5 mm/day). Although thermodynamic processes $\langle -\nabla \cdot \nabla q' \rangle$ and
 302 $\langle -\bar{\omega} \partial_p q' \rangle$ are weaker than dynamic processes, they also contributed to the extreme rainfall
 303 amounts. Evaporation E , for its part, contributed very little (0.1 mm/day). This is consistent with
 304 Cook et al. (2019) who found that rainfall anomalies in equatorial Central Africa do not depend
 305 directly on surface heating. It should also be noted that the residual term for a value of -1.2 mm/day
 306 is considerable. Indeed, the northward shift and strengthening of the northern component of the
 307 East African Jet (AEJ-N) in October are verified (Nicholson et al. 2022). This is illustrated by the

308 anomalous 700 hPa zonal wind in October 2019. In addition, the anomalous variance of the band-
309 pass filtered 700 hPa meridional wind over 2-6 days is also visible, indicating African easterly wave
310 activity (Reed et al., 1977). Other studies also point out that rainfall fluctuations in equatorial
311 Africa are associated with Kelvin waves (Jackson et al., 2019). The residual term could influence the
312 estimation of dynamic and thermodynamic distributions in the water budget, and its high values in
313 the Sahel region would be associated with a non-linear interaction between wind and changes in
314 humidity.

315 Analysis of the components of the water balance over the western part of the Congo Basin
316 (6°S-5°N, 6°-20°E) for October 2019 (Fig. 5b) shows that the increase in rainfall was dominated by
317 vertical advection of moisture induced by changes in vertical velocity $\langle -\omega' \partial_p \bar{q} \rangle$ (1.4 mm/day).
318 However, the contributions of the other processes, including the residual term, are low.

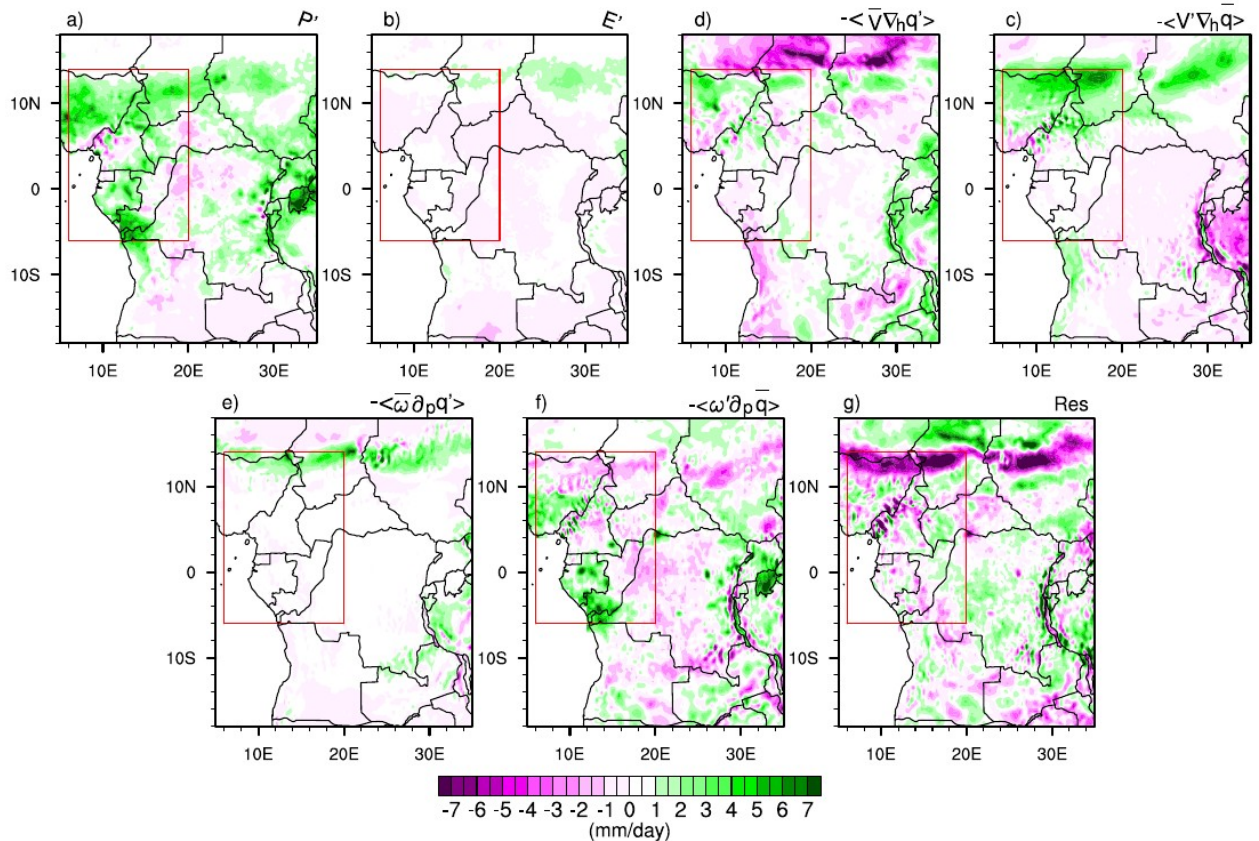
319



320

321 **Fig. 5** Monthly mean anomalies in moisture budget for October 2019, averaged in a) over the
 322 Northern part of West Central Africa (6°N-14°N, 6°-20°E) and b) over the Southern part of West
 323 Central Africa (6°S-5°N, 6°-20°E)

324 At the pixel scale, positive precipitation anomalies over eastern Nigeria, southern Chad and
 325 northern Cameroon (Fig. 6a) were mainly dominated by horizontal moisture advection induced by
 326 the horizontal wind anomaly (Fig. 6d). Over Gabon, south of Congo Brazzaville, positive
 327 precipitation anomalies were dominated by vertical moisture advection induced by vertical
 328 anomalous motion (Fig. 6f). Horizontal moisture advection induced by the specific humidity
 329 anomaly (Fig. 6c), although not the key factor associated with precipitation patterns, shows a small
 330 positive contribution over the northern part of the domain.



331
 332 **Fig. 6.** Spatial distributions of each term of the water budget equation during October 2019 over West
 333 Equatorial Africa (Red box). (a) Precipitation anomalies, (b) evaporation anomaly, (c) horizontal
 334 advection of anomalous moisture by climatological wind, (d) horizontal advection of climatological
 335 moisture by anomalous wind, (e) vertical advection of anomalous moisture by climatological vertical
 336 velocity, (f) vertical advection of climatological moisture by anomalous vertical velocity and (g) the
 337 residual term.

338

339 The contribution of evaporation (Fig. 6b) and horizontal advection of moisture induced by the
 340 specific humidity anomaly (Fig. 6e) remains weak over the entire domain, although some positive

341 values can be seen around 14°N. This result is similar to that provided by MERRA2 (Figure S2).
342 Thermodynamic effects reflect the change in the thermal state of the atmosphere associated with the
343 October 2019 rainfall extremes over West Central Africa. However, changes in the thermodynamic
344 effect, although not the key factor responsible for the October 2019 events, contributed up to 35%
345 of the total effect (the sum of dynamic and thermodynamic contributions) on the northern part and
346 15% on the southern part of the domain. This could be since the increase in diabatic heating
347 contributes to the change in the thermal state of the atmosphere, i.e. the increase in
348 thermodynamic effects (changes in humidity). In fact, Nicholson et al. (2022) reported that the
349 increase in SST in the tropical Atlantic strengthened the advection of moist air from the Atlantic
350 towards the region, with an increase in the moisture flux from the west to southwest.

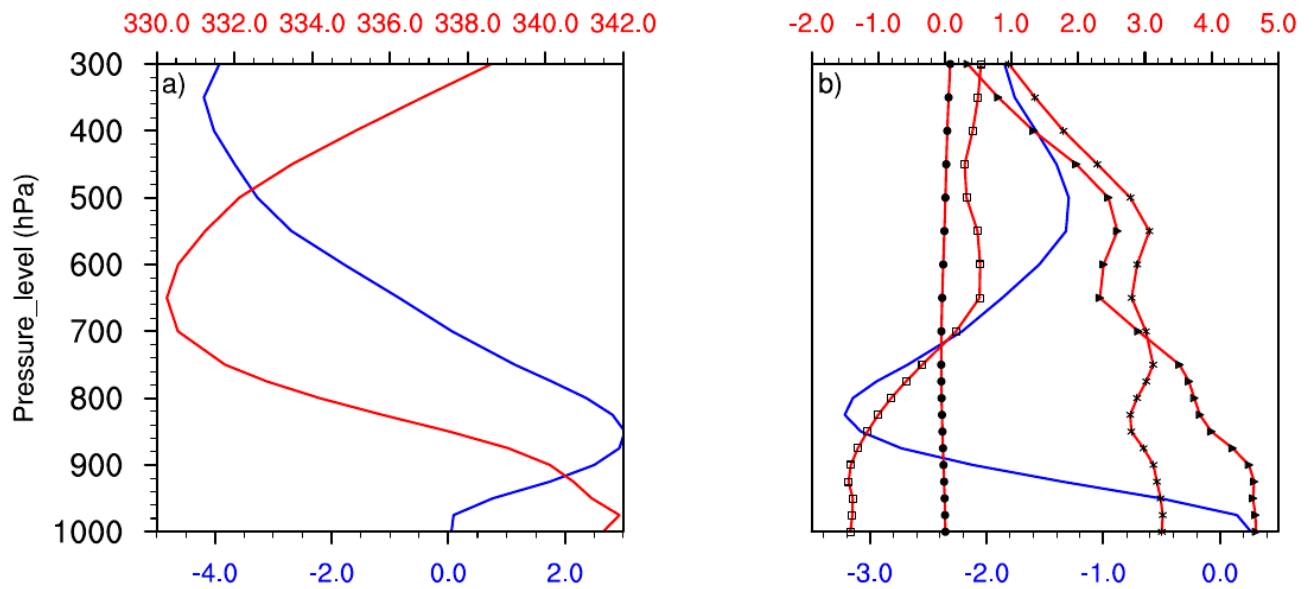
351

352 5 MSE budget analysis

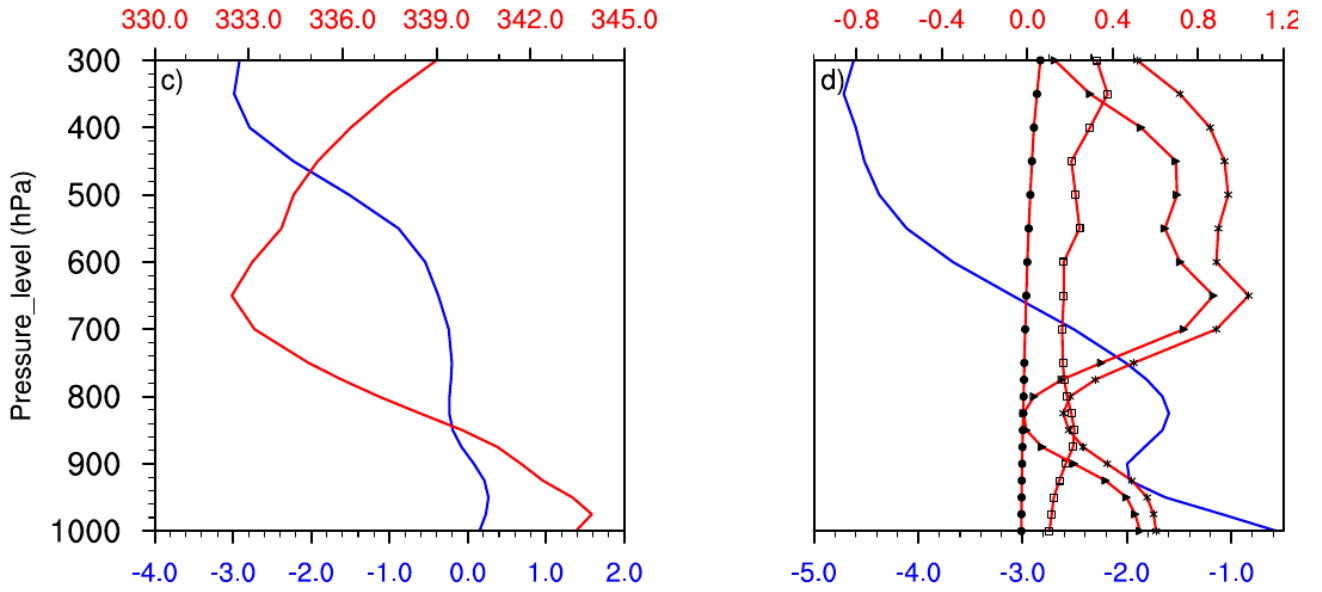
353 The previous results clearly showed that the vertical advection of moisture induced by the
354 vertical velocity anomaly was identified as the second dynamic parameter (after the horizontal
355 advection of moisture induced by the anomalous horizontal movement) contributing to the
356 increase in precipitation in October 2019. Diagnosis of the MSE budget, which takes account of the
357 thermal state of the atmosphere and the effect of atmospheric circulation, is used to analyse the
358 atmospheric perturbation related to moisture transport. The MSE largely influences the structure of
359 vertical motion. In addition, diagnosis of the MSE balance emphasises the relative contributions of
360 temperature, specific humidity and atmospheric circulation associated with the vertical motion
361 anomaly.

362 The vertical profiles of the vertical velocity anomaly ω' and the MSE climatology \bar{m}
363 averaged over the north of the domain are shown in Figure 7a. The vertical velocity anomaly ω'
364 shows positive values at the surface and negative values in the middle and upper troposphere. The
365 alternation of positive and negative values in the tropospheric column probably reduces the
366 contribution of the vertical advection of moisture induced by the anomalous vertical motion. The
367 MSE climatology \bar{m} exhibits a bottom-heavy structure with a minimum around 650 hPa. Such a
368 structure generally indicates that $\langle \partial_p \bar{m} \rangle < 0$ (Chen and Bordoni, 2014; Liu et al. 2021; Wen et al.
369 2022). As a result, positive (negative) values of $\langle \omega' \partial_p \bar{m} \rangle$ depends on the vertical structure of the
370 omega anomalies. The vertical velocity climatology $\bar{\omega}$ (Fig. 7b) is negative over the entire

371 troposphere, characterising an upward movement. The MSE anomaly m' decreased slightly near
 372 the surface then increased from 800 hPa to 550 hPa, with a minimum value around 550 hPa.
 373 However, this includes three terms, namely, gz' which is weak in the entire tropospheric column,
 374 the enthalpy anomaly $c_p T'$, which tends to increase, and $l_v q'$, tends to behave similarly to m'
 375 between 650 hPa and 300 hPa. To the south of the domain (Fig. 7c), the vertical velocity anomaly
 376 shows negative



377



378

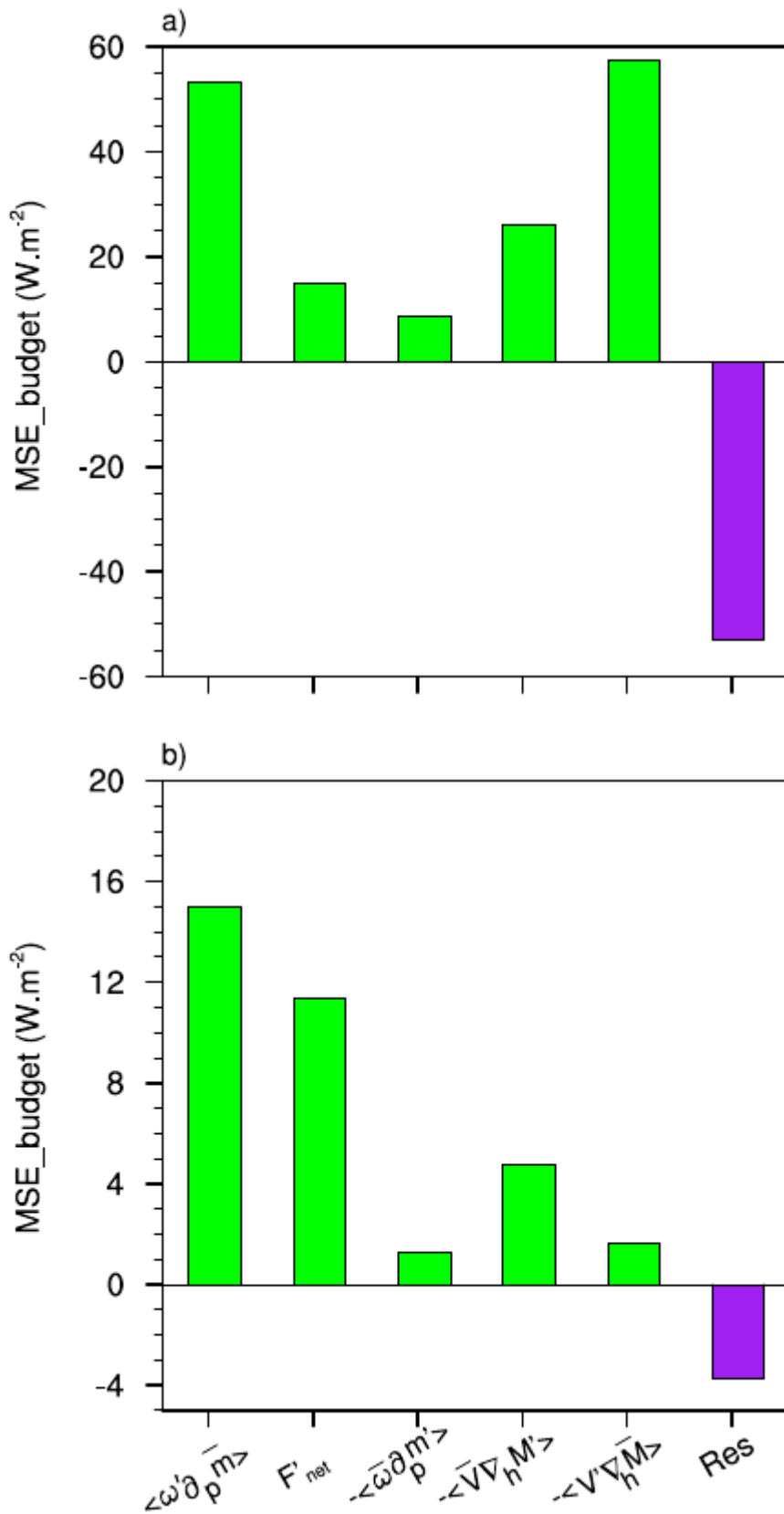
379 **Fig. 7.** Vertical profile of a) vertical velocity anomaly ω' (blue line: $10^{-2} Pa.s^{-1}$) and MSE
 380 climatology \bar{m} (red line: $10^3 J.Kq^{-1}$), and b) vertical velocity climatology $\bar{\omega}$ (blue line:
 381 $10^{-2} Pa.s^{-1}$), MSE anomaly m' (line with stars: $10^3 J.Kq^{-1}$), enthalpy anomaly $c_p T'$ (line with
 382 squares: $10^3 J.Kq^{-1}$), latent energy anomaly $l_v q'$ (line with triangles: $10^3 J.Kq^{-1}$) and
 383 geopotential anomaly Ψ' (line with dark circle: $10^3 J.Kq^{-1}$) averaged over the Northern part of
 384 West Central Africa (6°N-14°N, 6°-20°E) and c), d) the same parameters averaged over the
 385 Southern part of West Central Africa (6°S-5°N, 6°-20°E) during October 2019.

386

387 values from 900 hPa up to the upper troposphere, accelerating the anomalous vertical movement.
 388 The structure of the MSE climatology is similar to that observed to the north, with a maximum of
 389 around 650 hPa. The vertical profiles (Fig. 7d) of the MSE anomaly and the latent energy anomaly
 390 show similar structures throughout the tropospheric column, with maximum values at 650 hPa.

391 Based on the contributions of the different terms in equation 9 to the MSE over the northern
 392 part of West Central Africa (Fig. 8a), the advection of wet enthalpy induced by the horizontal wind
 393 anomalies $-\langle \mathbf{v}' \cdot \nabla M \rangle$ is the main term contributing most to the vertical advection of the MSE
 394 induced by the vertical velocity anomaly $\langle \omega' \partial_p \bar{m} \rangle$. This is confirmed by the high correlation ($r =$
 395 0.6) between the two terms compared to the other terms.

396 We also note the contribution of the thermodynamic terms, although the horizontal advection of the
397 MSE induced by the wet enthalpy variation $-\langle \nabla \cdot \nabla M' \rangle$ dominates ($r = 0.3$) compared to the
398 vertical advection of the MSE induced by the MSE variation $-\langle \omega \partial_p m' \rangle$ ($r = -0.2$). A weak
399 contribution from the net flow of energy is noticeable ($r = 0.18$). This could be due to the fact that
400 the energy in the radiative and turbulent heat fluxes penetrating the atmosphere over West Central
401 Africa has suffered a loss linked to the increase in cloud cover, which has a strong influence on
402 short-wave radiation. Such a reduction in energy in the air column has an impact on upward motion.
403 This result is in line with that of Wen et al. (2022) and Sheng et al. (2023), who pointed to a
404 reduction in the net energy in the air column during the exceptional rainy season in the summer of
405 2020 in the Yangtze River valley and the anomalous increase in precipitation over southern China
406 in 2022. However, as with the moisture balance, the residual term is also considerable.



407

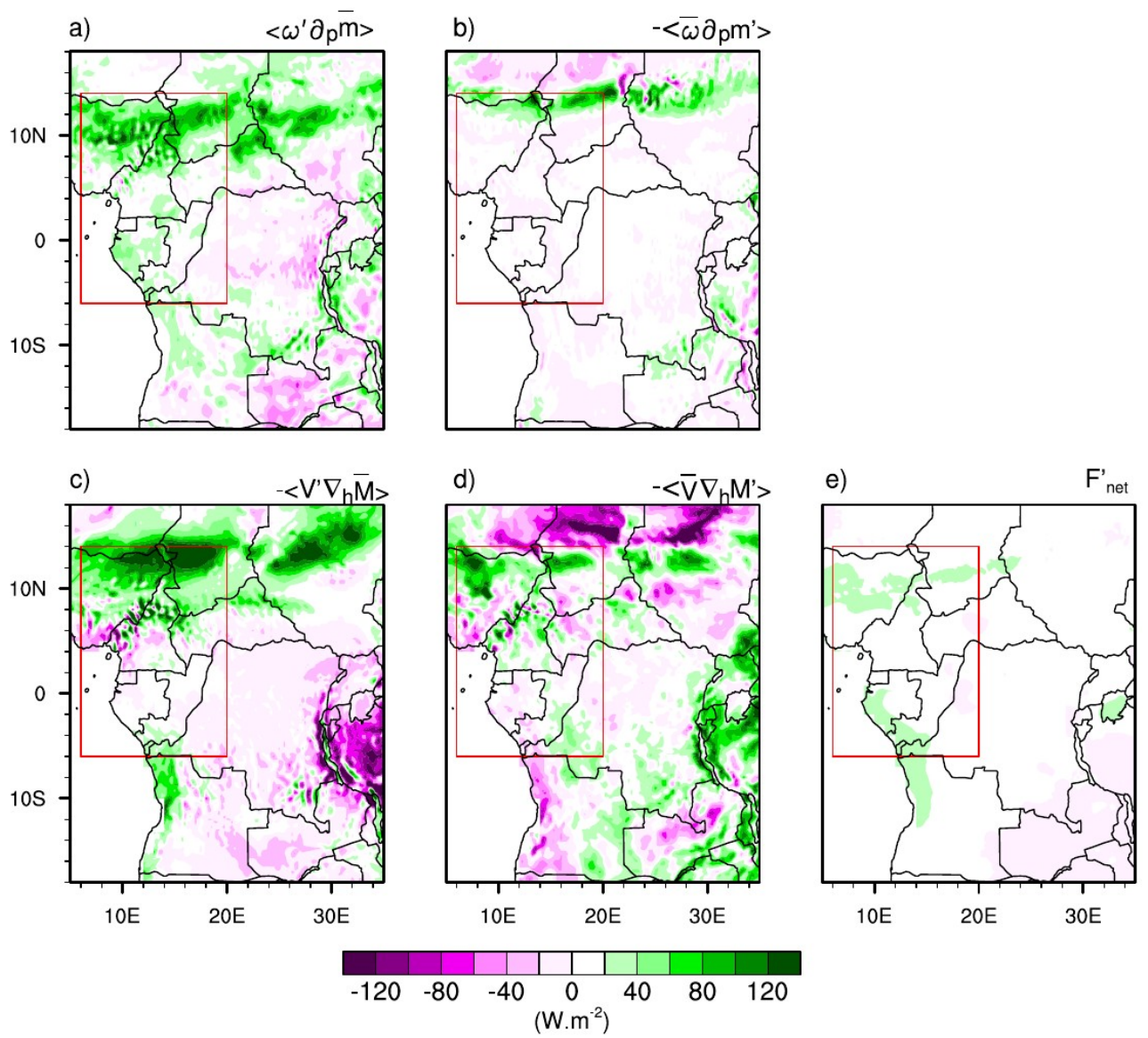
408 **Fig. 8.** Different terms of the Moist Static Energy (MSE) budget averaged in a) over the Northern
 409 part of West Central Africa (6°N-14°N, 6°-20°E) and b) over the Southern part of West Central
 410 Africa (6°S-5°N, 6°-20°E).

411

412 To the south of the domain(Fig. 8b), the increase in the net energy balance was responsible for
413 strengthening the vertical advection of the MSE induced by the vertical velocity anomaly ($r = 0.51$).

414 In addition, the increase in vertical movement was reinforced by an increase in the horizontal
415 advection of the MSE induced by the variation in wet enthalpy $-\langle \nabla \cdot \nabla M' \rangle$. This is in agreement
416 with the results of Kenfack et al. (2024) who highlighted the importance of horizontal advectons in
417 the MSE and moisture flux as well as their implications for vertical motion over the Congo Basin.
418 The contributions in vertical advection induced by changes in the MSE and horizontal advection
419 induced by changes in the horizontal wind are small. Moreover, similarly to the moisture flux
420 advected in the western part of the Congo Basin, the residual term was less important in the MSE
421 budget compared to the northern part.

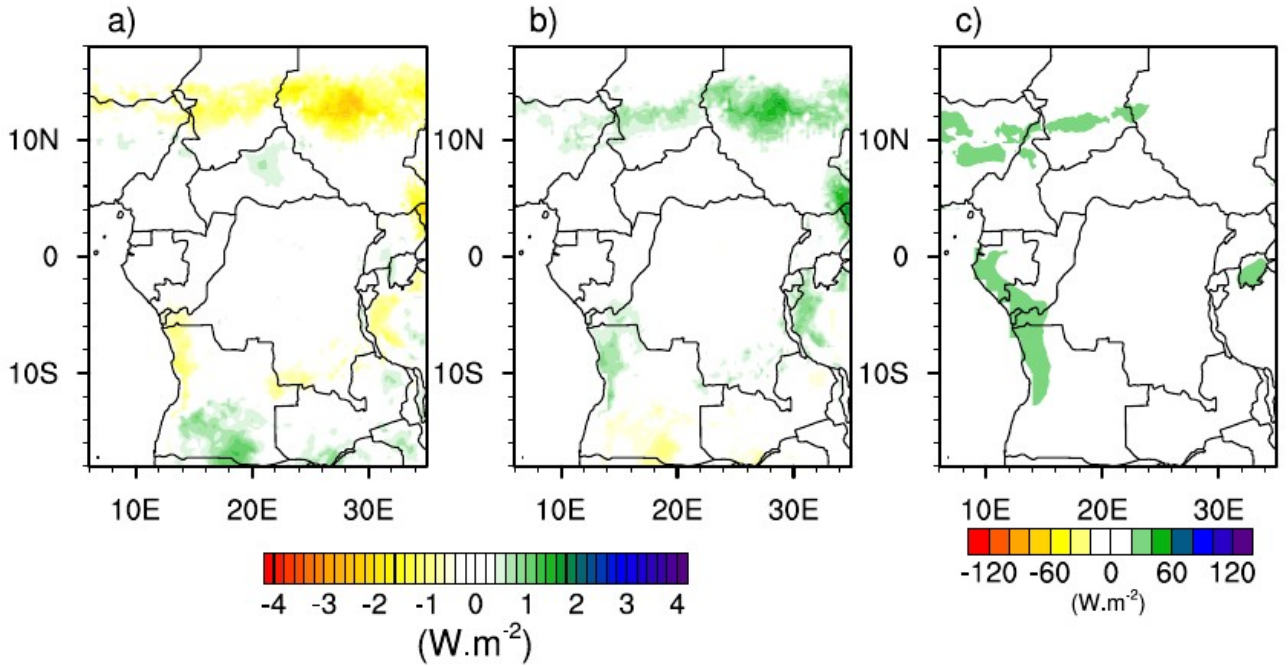
422 On a regional scale, the vertical advection of the MSE induced by the vertical motion anomaly
423 $\langle \omega' \partial_p \bar{m} \rangle$ (Fig. 9a) is mainly dominated by the dynamic term $-\langle \mathbf{V}' \cdot \nabla M \rangle$ (Fig. 9c), which brings



426 **Fig. 9.** Spatial distributions of each term of the Moist Static Energy (MSE) balance equation during
 427 October 2019 over West Equatorial Africa (Red box). (a) vertical advection of climatological MSE
 428 by anomalous vertical velocity, (b) vertical advection of anomalous MSE by climatological vertical
 429 velocity, (c) horizontal advection of anomalous moist enthalpy by climatological wind, (e) horizontal
 430 advection of climatological moist enthalpy by anomalous wind, and (f) net energy flux (at the surface
 431 and top of the atmosphere) in the atmospheric column.

432 There is a high concentration of positive values in both dynamic terms, up to $120 \text{ W}\cdot\text{m}^{-2}$ in the
 433 north of West Central Africa. In addition, the two thermodynamic terms $-\langle \omega \partial_p m' \rangle$ (Fig. 9b) and
 434 $-\langle \nabla \cdot \nabla M' \rangle$ (Fig. 9d), although weak, also contributed to reinforcing the vertical advection of
 435 MSE induced by the vertical motion anomaly. It should be remembered that the term $-\langle \omega \partial_p m' \rangle$
 436 remains very weak over the region as a whole, except the northern part where a slight layer of
 437 positive values can be observed. Terms $-\langle \mathbf{V}' \cdot \nabla M \rangle$, $-\langle \nabla \cdot \nabla M' \rangle$ and $-\langle \omega \partial_p m' \rangle$ in the MSE
 438 have a similar spatial distribution to terms $\langle -\mathbf{V}' \cdot \nabla \bar{q} \rangle$, $\langle -\nabla \cdot \nabla q' \rangle$ and $\langle -\bar{\omega} \partial_p q' \rangle$ in the
 439 moisture, which is in agreement with the findings of Kenfack et al. (2024). The difference between
 440 the net energy balance for 2019 and the climatology (Fig. 9e) shows low positive values in the north
 441 and south of the region respectively. Such an increase (mainly to the south of the area) is associated
 442 with a strengthening in the vertical structure of the MSE anomaly through ascending currents and,
 443 consequently, an increase in precipitation. A further analysis of the net energy balance (Fig. 10)
 444 shows that during October 2019, the latent heat flux (Fig. 10a) decreased mainly over the Sahel and
 445 to the south of the domain. Sensible heat, on the other hand, increased slightly, with values of
 446 around $1.5 \text{ W}\cdot\text{m}^{-2}$. Analysis of the radiative flux anomalies shows strong positive values over the
 447 Sahel and the southern part of the domain (up to $50 \text{ W}\cdot\text{m}^{-2}$), showing that this is the main factor
 448 responsible for the increase in the energy balance during the exceptional event of October 2019.

449



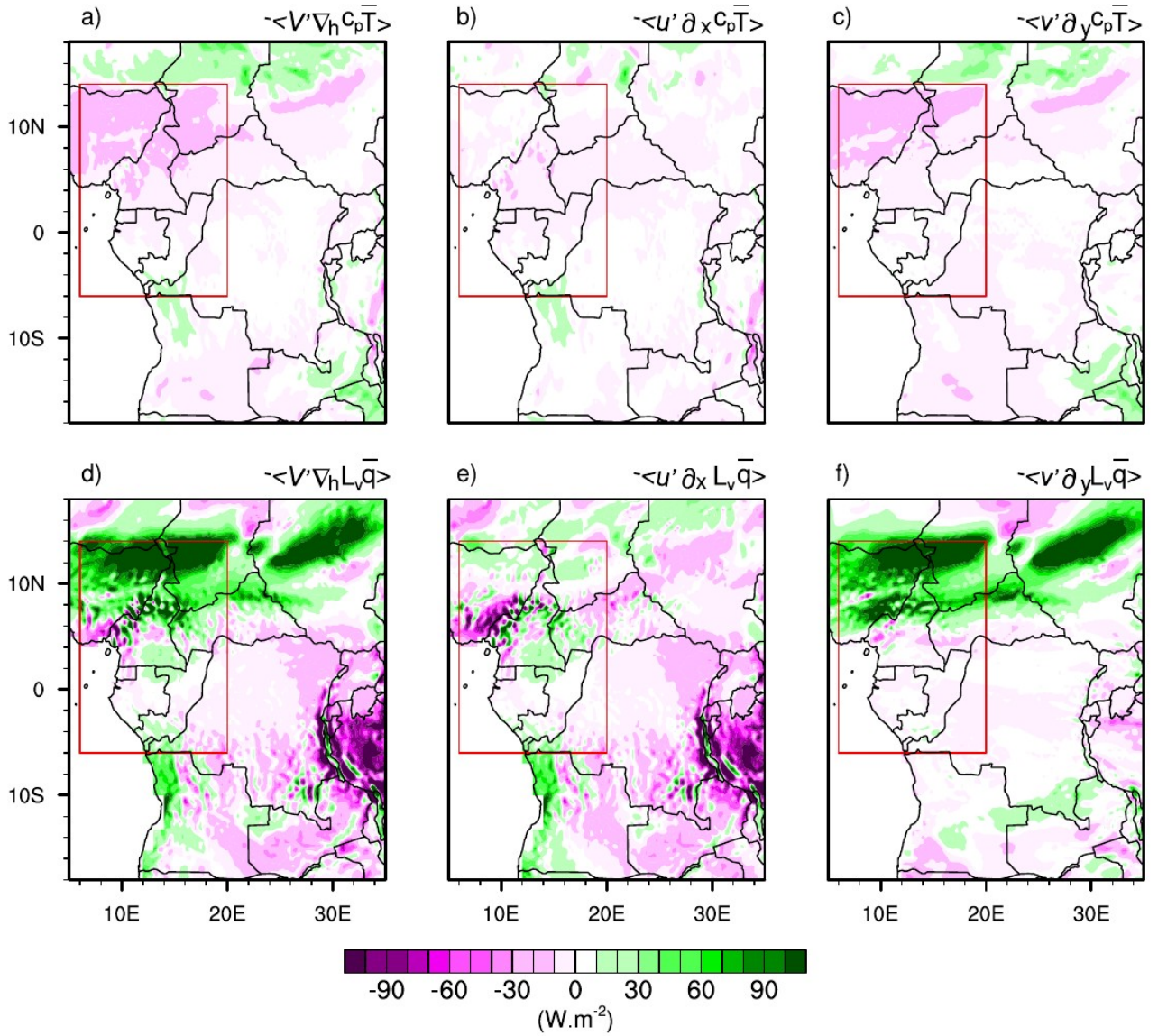
450

451 **Fig. 10.** Spatial distribution of a) latent heat, b) sensible heat and c) radiative flux anomalies in
 452 October 2019 over western equatorial Africa.

453 Although the dynamic contribution is the most important, the thermodynamic contribution cannot
 454 be neglected. This would mean that the interaction between atmospheric dynamic and
 455 thermodynamic variables would induce significant indirect effects on October 2019 precipitation
 456 anomalies over West Central Africa.

457 5.1 Dynamic effect

458 The aforementioned results clearly show that enthalpy advection induced by the horizontal wind
 459 anomaly is crucial in understanding the processes at the origin of October 2019 extreme
 460 precipitation over northern part of West Central Africa. It should be remembered that, as we
 461 mentioned in the diagnostic section of the MSE balance, the wet enthalpy $M = c_p T + L_v q$ results
 462 from the sum of the dry enthalpy and the latent heat. Thus, the horizontal advection of wet enthalpy
 463 induced by the wind anomaly can be separated into two terms: dry enthalpy $-\langle \mathbf{V}' \cdot \nabla_h c_p T \rangle$ (Fig.
 464 11a) and latent heat $-\langle \mathbf{V}' \cdot \nabla_h L_v \bar{q} \rangle$ (Fig. 11d).



465

466 **Fig. 11.** Horizontal advection of (a–c) climatological dry enthalpy and (d–f) latent energy by
 467 anomalous wind, designated as a dynamic effect during October 2019 over West Central Africa
 468 (Red box). (a, d) Total advection, (b, e) zonal component, and (c, f) meridional component.

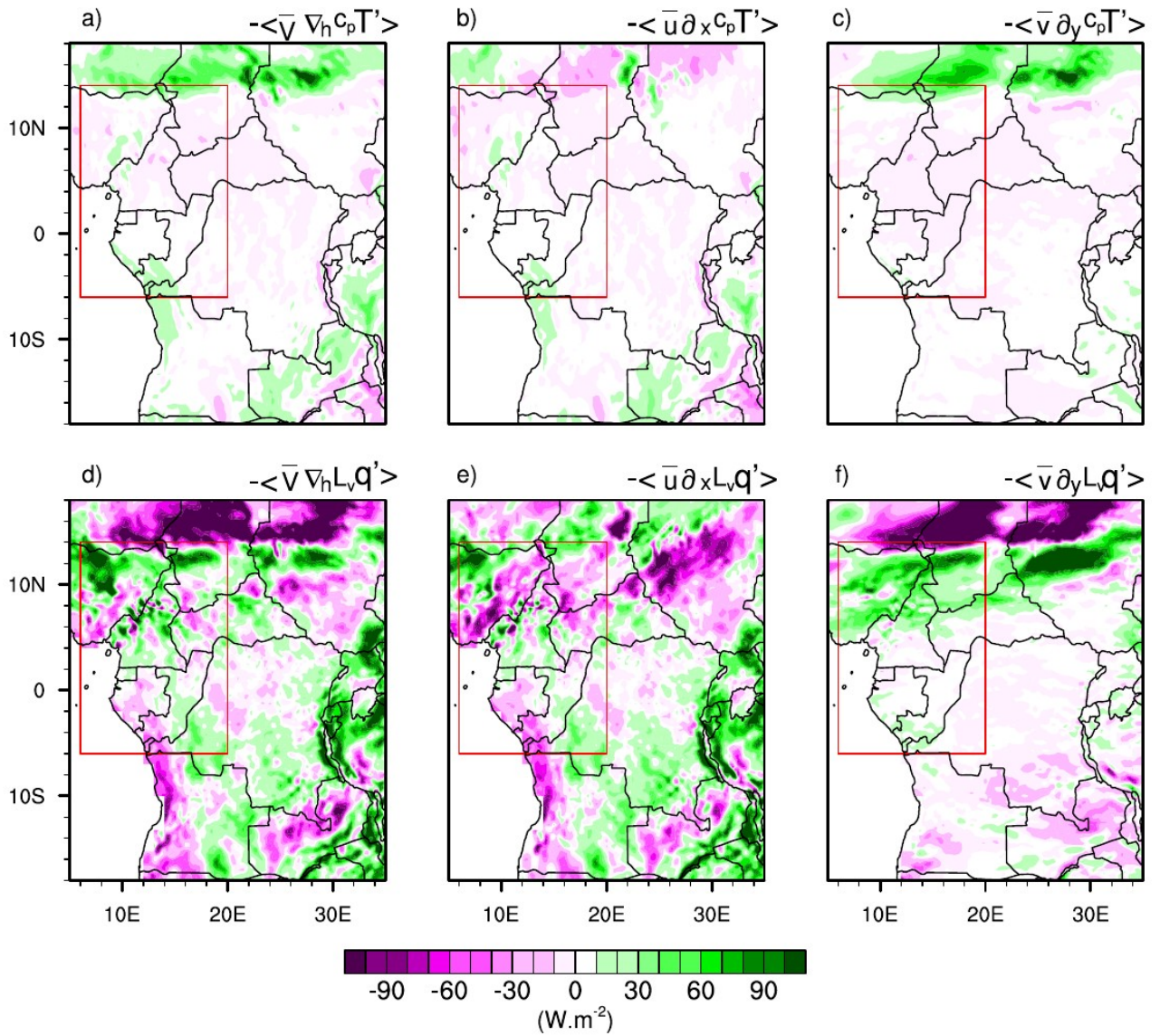
469

470 Given the influence of the wind anomaly components on the displacement of dry enthalpy and
 471 latent heat, a further decomposition of the $-\langle \mathbf{V}' \cdot \nabla_h c_p \bar{T} \rangle$ and $-\langle \mathbf{V}' \cdot \nabla_h l_v \bar{q} \rangle$ terms along the
 472 zonal (Figs. 11b,e) and meridional (Figs. 11c,f) directions appear necessary. Figure 11a shows that
 473 the advection of dry enthalpy induced by the horizontal wind anomaly decreased over the area-
 474 averaged, with the highest values between 6°N and 14°N. The advection of dry enthalpy by the
 475 meridional wind anomaly (Fig. 11c) is particularly responsible for the decrease in the

476 $-\langle \mathbf{V}' \cdot \nabla_h c_p T' \rangle$ term compared with the advection of dry enthalpy induced by the zonal wind
477 anomaly (Fig. 11b), which is weak. For the transport of latent heat (Fig. 11d), the influence of the
478 advection of $-\langle \mathbf{V}' \cdot \nabla_h l_v \bar{q}' \rangle$ term under the effect of the anomalous meridional circulation is the
479 main term responsible for the supply of moist air to the northern part of the area, while the low
480 contribution to the south is associated with a low input of moist air from the zonal wind anomaly
481 (Fig. 11f). Analysis of the advection of dry enthalpy and latent heat by anomalous winds shows that
482 the meridional wind anomaly had a significant impact compared with the zonal wind anomaly. In
483 addition, the advection of the dynamic term associated with latent heat contributed significantly to
484 the supply of MSE to West Central Africa compared to the advection of the dynamic term
485 associated with dry enthalpy. One of the reasons would be because in addition to the warm Atlantic
486 SSTs, there was also an anomalous meridional mean sea level pressure (MSLP) gradient in the
487 Central African Sahel between a lower MSLP over the eastern Sahara and a higher pressure
488 between 10 and 15°N. In addition, the trans-equatorial meridional wind fluctuated with the activity
489 of the African easterly waves over the Gulf of Guinea (Nicholson et al. 2022).

490 5.2 Thermodynamic effect

491 The results of the previous section highlighted the importance of dynamics, particularly in a
492 meridional direction, on extreme precipitation in October 2019. However, we previously also
493 observed that the thermodynamic contribution should not be neglected. Similar to the previous
494 section, the thermodynamic term $-\langle \mathbf{V}' \cdot \nabla M' \rangle$ (i.e. the advection of the wet enthalpy anomaly
495 associated with wind climatology) can also be separated into two terms, namely: Dry enthalpy
496 $-\langle \mathbf{V}' \cdot \nabla_h c_p T' \rangle$ (Fig. 12a) and latent heat $-\langle \mathbf{V}' \cdot \nabla_h l_v \bar{q}' \rangle$ (Fig. 12d).



497

498 **Fig. 12.** As in Fig. 11, but for the thermodynamic effect (horizontal advection of anomalous dry
 499 enthalpy and latent energy by climatological wind) during October 2019 over West Central Africa
 500 (Red box).

501

502 To better assess the contribution of each term, we split the horizontal wind into zonal and
 503 meridional directions. The advection of the dry enthalpy anomaly by the horizontal zonal and
 504 meridional wind components is shown in Figures 12b and 12c, respectively. It can also be seen that
 505 the dry enthalpy anomaly is very small over the whole area. On the other hand, the advection of the
 506 latent heat anomaly by the horizontal wind climatology is more pronounced. Variations in latent
 507 heat are strong in the meridional direction, while the zonal direction shows a reduction in abnormal
 508 latent heat. This could be due to the strong meridional wind associated with the increase in SST in

509 the tropical Atlantic, which results in strong advection of water vapor into West Central Africa,
510 leading to precipitation. The reduction in advection of the latent heat anomaly on the Atlantic coast
511 is amplified by the zonal wind climatology. However, the advection of the wet enthalpy induced by
512 the horizontal wind anomaly (dynamic effect) is stronger than the advection of the wet enthalpy
513 anomaly by the wind climatology. As a result, we note in particular the changes in the meridional
514 wind for the dynamic effect and the latent heat associated with the warming of the equatorial
515 Atlantic for the thermodynamic effect.

516 **6 Summary and concluding remarks**

517 West Central Africa was hit by unprecedented exceptional rainfall in October 2019. A few
518 studies have investigated the meteorological causes associated with these extreme rainfall events
519 (Wainwright et al, 2020; Nicholson et al. 2022). This study followed these perspectives and focused
520 on evaluating the dynamic and thermodynamic processes that controlled the extreme events of
521 2019. We proceeded by decomposing the water balance and MSE equation, separating the
522 associated dynamic and thermodynamic effects. Changes in atmospheric circulation are behind
523 dynamic processes, while changes in water vapor are behind thermodynamic processes. This
524 approach provides a better understanding of the mechanisms behind rainfall anomalies.. The main
525 findings can be summarised as follows:

- 526 1. The main feature of October 2019 in the northern part of the area was a strong southerly
527 circulation compared with the typical climatology for 1988-2017. In addition, a more
528 pronounced rate of humidity associated with significant diabatic heating over West Central
529 Africa up to 15°N was recorded.
- 530 2. The diagnosis of the water balance reveals that the exceptional rainfall in October 2019 was
531 mainly dominated by dynamic effects. However, moisture advection induced by horizontal
532 wind anomalies is the dominant process of precipitation anomalies over the northern part of
533 the zone, while vertical moisture advection induced by vertical velocity anomalies is the
534 dominant process of precipitation extremes in the south, mainly over Gabon and southern
535 Congo Brazzaville. Changes in the thermodynamic effect, although not the key factor
536 responsible for the events of October 2019, contribute up to 35% of the total effect (the sum
537 of the dynamic and thermodynamic contributions) on the northern part and 15% on the
538 southern part of the domain. The contribution of evaporation remains weak in both areas
539 combined, which allows us to conclude that evaporation was not responsible for the heavy
540 rainfall of October 2019 in West Central Africa.

541 3. The MSE vertical advection anomaly is dominated over the northern part of the area by the
542 dynamic term (i.e. the advection of the wet enthalpy induced by the horizontal wind
543 anomalies) compared to the thermodynamic terms (i.e. the horizontal advection of the MSE
544 induced by the variation of the wet enthalpy and the vertical advection of the MSE induced
545 by the variation of the MSE). In the southern part, the increase in the net energy balance
546 compared with the climatology is the dominant process that has contributed most to the
547 change in the structure of the vertical anomaly of the MSE. The prevailing net balance is
548 controlled by the anomalies in radiative flux compared with the anomalies in latent and
549 sensible heat flux. An extended analysis shows that these variations in the MSE over the
550 north of West Central Africa were governed by its meridional component, in particular the
551 variations in the meridional wind in the dynamic effect and the meridional variations in
552 latent heat in the thermodynamic effect. It should be pointed out that in both cases, the
553 contribution of dry enthalpy helped to reduce the dynamic term and was small in the
554 thermodynamic term.

555 The results of this study show that moisture advection induced by horizontal wind anomalies and
556 vertical moisture advection induced by vertical velocity anomaly were crucial mechanisms in the
557 anomalous October 2019 exceptional rainfall increase over West Central Africa. In addition,
558 changes in the MSE budget, mainly through the meridional circulation (dynamic effect), and latent
559 heat (thermodynamic effect) also played an important role in the northern part of the area, while the
560 increase in the energy balance contributed considerably to the change in the MSE balance in the
561 southern part of the area. However, there was little contribution from dry enthalpy. These results are
562 consistent with those of Nicholson et al (2022) who showed that the increase in equatorial Atlantic
563 SSTs associated with the late retreat of the West African monsoon played an important role in
564 precipitation anomalies in the Sahel. Changes in SSTs along the east coast of the equatorial Atlantic
565 display a similar pattern to the Atlantic Niño as described by Lutz et al. (2013). Furthermore,
566 Vallès-Casanova et al (2020) also highlighted the fact that 2019 was characterised by a particularly
567 intense Atlantic Niño, which lasted until October, placing the dynamic and thermodynamic
568 processes in the context of the large-scale circulation. The importance of the dynamic contribution
569 during extreme precipitation events has been reported in other regions, notably over southern China
570 (Wen et al. 2022; Sheng et al. 2023). This calls for comprehensive evaluations of both dynamic and
571 thermodynamic contributions, and their possible feedback, to assess the potential impact of climate
572 change on extreme precipitation events in this region.

573

574

575 **Code availability**

576 Figures shown in this study are plotted using the NCAR Command Language (NCL,
577 <https://doi.org/10.5065/D6WD3XH5>, The NCAR Command Language, 2017). Codes can be
578 obtained from the corresponding author.

579

580 **Data Availability Statement**

581

582 The **ERA5** reanalysis is produced within the Copernicus Climate Change Service (C3S) by the
583 ECMWF and is accessible via the link [https://cds.climate.copernicus.eu/cdsapp#!/dataset/reanalysis-](https://cds.climate.copernicus.eu/cdsapp#!/dataset/reanalysis-era5-pressure-levels-monthly-means?tab=1/4form)
584 [era5-pressure-levels-monthly-means?tab=1/4form](https://cds.climate.copernicus.eu/cdsapp#!/dataset/reanalysis-era5-pressure-levels-monthly-means?tab=1/4form).

585

586 **Acknowledgements.** The authors thank all the observational and reanalysis data providers used in
587 this study, and the research of the International Joint Laboratory “Dynamics of Terrestrial
588 Ecosystems in Central Africa: A Context of Global Changes” (IJL DYCOCA/LMI DYCOFAC).

589

590 **Competing Interests.** The authors declare that they have no conflict of interest.

591

592 **Authors' contributions**

593 **kK:** Conceptualization; data analysis; formal analysis; investigation; methodology; writing - original
594 draft; review and editing.

595 **FM:** Supervision; conceptualization; investigation; writing – review and editing.

596 **ZYD:** Investigation; writing; review and editing; supervision; validation.

597 **LADT:** Validation; supervision; methodology; writing – review and editing.

598 **ATT:** Conceptualization; investigation; methodology; project administration; resources; supervision;
599 validation; review and editing.

600 **DAV:** Project administration; supervision; resources; validation; methodology; writing – review and
601 editing.

602

603 **Funding.** Not applicable

604

605 **References**

606

608 Andrews, P. C., Cook, K. H., and Vizy, E. K.: Mesoscale convective systems in the Congo Basin:
609 Seasonality, regionality, and diurnal cycles, *Clim. Dynam.*, 62, 609–630,
610 <https://doi.org/10.1007/s00382-023-06903-7>, 2023.

611

612 Kenya – over 100 dead, 18,000 displaced after recent floods and landslides – floodlist:
613 <http://floodlist.com/africa/kenya-floods-november-2019>, last access: 2 April 2024.

614

615 Aretouyap, Z., Kemgang, F. E. G., Domra, J. K., Bisso, D., and Njandjock, P. N.: Understanding the
616 occurrences of fault and landslide in the region of West-Cameroon using remote sensing and GIS
617 techniques, *Nat. Hazards*, 109, 1589–1602, <https://doi.org/10.1007/s11069-021-04890-8>, 2021.

618

619 Bell, J. P., Tompkins, A. M., Bouka-Biona, C., and Sanda, I. S.: A process-based investigation into
620 the impact of the Congo basin deforestation on surface climate, *J. Geophys. Res-Atmos.*, 120, 5721–
621 5739, <https://doi.org/10.1002/2014jd022586>, 2015.

622

623 Black, E.: The relationship between Indian Ocean sea–surface temperature and East African rainfall,
624 *Philos. T. R. Soc. A*, 363, 43–47, <https://doi.org/10.1098/rsta.2004.1474>, 2005.

625

626 Chadwick, R., Good, P., and Willett, K.: A simple moisture advection model of specific humidity
627 change over land in response to SST warming, *J. Climate*, 29, 7613–7632,
628 <https://doi.org/10.1175/jcli-d-16-0241.1>, 2016.

629

630 Chen, J. and Bordoni, S.: Orographic effects of the Tibetan plateau on the east Asian summer
631 monsoon: An energetic perspective, *J. Climate*, 27, 3052–3072, <https://doi.org/10.1175/jcli-d-13-00479.1>, 2014.

633

634 Cook, K. H. and Vizy, E. K.: Hydrodynamics of regional and seasonal variations in Congo Basin
635 precipitation, *Clim. Dynam.*, 59, 1775–1797, <https://doi.org/10.1007/s00382-021-06066-3>, 2021.

636

637 Cook, K. H., Liu, Y., and Vizy, E. K.: Congo Basin drying associated with poleward shifts of the

638 African thermal lows, *Clim. Dynam.*, 54, 863–883, <https://doi.org/10.1007/s00382-019-05033-3>,
639 2019.
640
641 Dyer, E. L. E., Jones, D. B. A., Nusbaumer, J., Li, H., Collins, O., Vettoretti, G., and Noone, D.:
642 Congo Basin precipitation: Assessing seasonality, regional interactions, and sources of moisture, *J.*
643 *Geophys. Res-Atmos.*, 122, 6882–6898, <https://doi.org/10.1002/2016jd026240>, 2017.
644
645 Fontaine, B., Roucou, P., and Trzaska, S.: Atmospheric water cycle and moisture fluxes in the West
646 African monsoon: Mean annual cycles and relationship using NCEP/NCAR reanalysis, *Geophys.*
647 *Res. Lett.*, 30, <https://doi.org/10.1029/2002gl015834>, 2003.
648
649 Fotso-Nguemo, T. C., Chamani, R., Yepdo, Z. D., Sonkoué, D., Matsaguim, C. N., Vondou, D. A.,
650 and Tanessong, R. S.: Projected trends of extreme rainfall events from CMIP5 models over Central
651 Africa, *Atmos. Sci. Lett.*, 19, <https://doi.org/10.1002/asl.803>, 2018.
652
653 Fotso-Nguemo, T. C., Diallo, I., Diakhaté, M., Vondou, D. A., Mbaye, M. L., Haensler, A., Gaye, A.
654 T., and Tchawoua, C.: Projected changes in the seasonal cycle of extreme rainfall events from
655 CORDEX simulations over Central Africa, *Climatic. Change*, 155, 339–357,
656 <https://doi.org/10.1007/s10584-019-02492-9>, 2019.
657
658 Funk, C., Peterson, P., Landsfeld, M., Pedreros, D., Verdin, J., Shukla, S., Husak, G., Rowland, J.,
659 Harrison, L., Hoell, A., and Michaelsen, J.: The climate hazards infrared precipitation with stations—
660 a new environmental record for monitoring extremes, *Scientific Data*, 2,
661 <https://doi.org/10.1038/sdata.2015.66>, 2015.
662
663 Garcin, Y., Deschamps, P., Ménot, G., de Saulieu, G., Schefuß, E., Sebag, D., Dupont, L. M.,
664 Oslisly, R., Brademann, B., Mbusnum, K. G., Onana, J.-M., Ako, A. A., Epp, L. S., Tjallingii, R.,
665 Strecker, M. R., Brauer, A., and Sachse, D.: Early anthropogenic impact on Western Central African
666 rainforests 2,600 y ago, *P. Natl. A. Sci. India. A*, 115, 3261–3266,
667 <https://doi.org/10.1073/pnas.1715336115>, 2018.
668
669 Gelaro, R., McCarty, W., Suárez, M. J., Todling, R., Molod, A., Takacs, L., Randles, C. A.,
670 Darmenov, A., Bosilovich, M. G., Reichle, R., Wargan, K., Coy, L., Cullather, R., Draper, C.,
671 Akella, S., Buchard, V., Conaty, A., da Silva, A. M., Gu, W., Kim, G.-K., Koster, R., Lucchesi, R.,

672 Merkova, D., Nielsen, J. E., Partyka, G., Pawson, S., Putman, W., Rienecker, M., Schubert, S. D.,
673 Sienkiewicz, M., and Zhao, B.: The Modern-Era Retrospective Analysis for Research and
674 Applications, Version 2 (MERRA-2), *J. Climate*, 30, 5419–5454, [https://doi.org/10.1175/jcli-d-16-](https://doi.org/10.1175/jcli-d-16-0758.1)
675 0758.1, 2017.

676

677

678 Gou, Y., Balling, J., De Sy, V., Herold, M., De Keersmaecker, W., Slagter, B., Mullissa, A., Shang,
679 X., and Reiche, J.: Intra-annual relationship between precipitation and forest disturbance in the
680 African rainforest, *Environ. Res. Lett.*, 17, 044044, <https://doi.org/10.1088/1748-9326/ac5ca0>, 2022.

681

682 Harris, I., Osborn, T. J., Jones, P., and Lister, D.: Version 4 of the CRU TS monthly high-resolution
683 gridded multivariate climate dataset, *Scientific Data*, 7, <https://doi.org/10.1038/s41597-020-0453-3>,
684 2020.

685

686 He, Y., Tian, W., Huang, J., Wang, G., Ren, Y., Yan, H., Yu, H., Guan, X., and Hu, H.: The
687 mechanism of increasing summer water vapor over the Tibetan plateau, *J. Geophys. Res-Atmos.*,
688 126, <https://doi.org/10.1029/2020jd034166>, 2021.

689

690 Hersbach, H., Bell, B., Berrisford, P., Hirahara, S., Horányi, A., Muñoz-Sabater, J., Nicolas, J.,
691 Peubey, C., Radu, R., Schepers, D., Simmons, A., Soci, C., Abdalla, S., Abellan, X., Balsamo, G.,
692 Bechtold, P., Biavati, G., Bidlot, J., Bonavita, M., De Chiara, G., Dahlgren, P., Dee, D., Diamantakis,
693 M., Dragani, R., Flemming, J., Forbes, R., Fuentes, M., Geer, A., Haimberger, L., Healy, S., Hogan,
694 R. J., Hólm, E., Janisková, M., Keeley, S., Laloyaux, P., Lopez, P., Lupu, C., Radnoti, G., de Rosnay,
695 P., Rozum, I., Vamborg, F., Villaume, S., and Thépaut, J.: The ERA5 global reanalysis, *Q. J. Roy.*
696 *Meteor. Soc.*, 146, 1999–2049, <https://doi.org/10.1002/qj.3803>, 2020.

697

698 Hua, W., Zhou, L., Nicholson, S. E., Chen, H., and Qin, M.: Assessing reanalysis data for
699 understanding rainfall climatology and variability over Central Equatorial Africa, *Clim. Dynam.*, 53,
700 651–669, <https://doi.org/10.1007/s00382-018-04604-0>, 2019.

701

702 Huffman, G. J., Adler, R. F., Bolvin, D. T., and Gu, G.: Improving the global precipitation record:
703 GPCP Version 2.1, *Geophys. Res. Lett.*, 36, <https://doi.org/10.1029/2009gl040000>, 2009.

704

705 Jackson, B., Nicholson, S. E., and Klotter, D.: Mesoscale convective systems over Western

706 Equatorial Africa and their relationship to large-scale circulation, *Mon. Weather. Rev.*, 137, 1272–
707 1294, <https://doi.org/10.1175/2008mwr2525.1>, 2009.

708

709 Jiang, J., Zhou, T., Chen, X., and Zhang, L.: Future changes in precipitation over Central Asia based
710 on CMIP6 projections, *Environ. Res. Lett.*, 15, 054009, <https://doi.org/10.1088/1748-9326/ab7d03>,
711 2020.

712

713 Johannsen, Ermida, Martins, Trigo, Nogueira, and Dutra: Cold bias of ERA5 summertime daily
714 maximum land surface temperature over Iberian Peninsula, *Remote. Sens-Basel*, 11, 2570,
715 <https://doi.org/10.3390/rs11212570>, 2019.

716

717 Kamae, Y., Mei, W., and Xie, S.-P.: Climatological relationship between warm season atmospheric
718 rivers and heavy rainfall over East Asia, *J. Meteorol. Soc. Jpn., Ser. II*, 95, 411–431,
719 <https://doi.org/10.2151/jmsj.2017-027>, 2017.

720

721 Kenfack, K., Tamoffo, A. T., Djiotang Tchotchou, L. A., and Vondou, D. A.: Assessment of
722 uncertainties in reanalysis datasets in reproducing thermodynamic mechanisms in the moisture
723 budget's provision in the Congo Basin, *Theor. Appl. Climatol.*, 154, 613–626,
724 <https://doi.org/10.1007/s00704-023-04576-0>, 2023.

725

726 Kenfack, K., Tamoffo, A. T., Tchotchou, L. A. D., Marra, F., Kaissassou, S., Nana, H. N., and
727 Vondou, D. A.: Processes behind the decrease in Congo Basin precipitation during the rainy seasons
728 inferred from ERA-5 reanalysis, *Int. J. Climatol.*, <https://doi.org/10.1002/joc.8410>, 2024.

729

730 Kuete, G., Pokam Mba, W., and Washington, R.: African Easterly Jet South: Control, maintenance
731 mechanisms and link with Southern subtropical waves, *Clim. Dynam.*, 54, 1539–1552,
732 <https://doi.org/10.1007/s00382-019-05072-w>, 2019.

733

734 Li, P., Zhou, T., and Chen, X.: Water vapor transport for spring persistent rains over southeastern
735 China based on five reanalysis datasets, *Clim. Dynam.*, 51, 4243–4257,
736 <https://doi.org/10.1007/s00382-017-3680-3>, 2017.

737

738 Liu, S., Wen, N., and Li, L.: Dynamic and thermodynamic contributions to Northern China dryness
739 in El Niño developing summer, *Int. J. Climatol.*, 41, 2878–2890, <https://doi.org/10.1002/joc.6995>,

740 2021.
741
742 Longandjo, G.-N. T. and Rouault, M.: Revisiting the seasonal cycle of rainfall over Central Africa, *J.*
743 *Climate*, 37, 1015–1032, <https://doi.org/10.1175/jcli-d-23-0281.1>, 2024.
744
745 Lutz, K., Rathmann, J., and Jacobeit, J.: Classification of warm and cold water events in the eastern
746 tropical Atlantic Ocean, *Atmos. Sci. Lett.*, 14, 102–106, <https://doi.org/10.1002/asl2.424>, 2013.
747
748 Mariotti, L., Diallo, I., Coppola, E., and Giorgi, F.: Seasonal and intraseasonal changes of African
749 monsoon climates in 21st century CORDEX projections, *Climatic. Change*, 125, 53–65,
750 <https://doi.org/10.1007/s10584-014-1097-0>, 2014.
751
752 Marra, F., Levizzani, V., and Cattani, E.: Changes in extreme daily precipitation over Africa: Insights
753 from a non-asymptotic statistical approach, *J. Hydrol. X*, 16, 100130,
754 <https://doi.org/10.1016/j.hydroa.2022.100130>, 2022.
755
756 Moon, S. and Ha, K.-J.: Future changes in monsoon duration and precipitation using CMIP6, *NPJ*
757 *Clim. Atmos. S.*, 3, <https://doi.org/10.1038/s41612-020-00151-w>, 2020.
758
759 Moudi Pascal, I., Kammalac Jores, T., Talib, J., Appolinaire, V. D., Hirons, L., Christian, N., Tene
760 Romeo-Ledoux, D., Fogang Michael, T., Marceline, M., Tanessong Roméo, S., Dione, C.,
761 Thompson, E., Salih, A. A. M., and Ngaryamgaye, S.: Strengthening weather forecast and
762 dissemination capabilities in Central Africa: Case assessment of intense flooding in January 2020,
763 *Climate Services*, 32, 100411, <https://doi.org/10.1016/j.cliser.2023.100411>, 2023.
764
765 Nana, H. N., Tanessong, R. S., Tchotchou, L. A. D., Tamoffo, A. T., Moihamette, F., and Vondou,
766 D. A.: Influence of strong South Atlantic Ocean Dipole on the Central African rainfall's system,
767 *Clim. Dynam.*, 62, 1–16, <https://doi.org/10.1007/s00382-023-06892-7>, 2023.
768
769 Neelin, J. D.: Moist dynamics of tropical convection zones in monsoons, teleconnections, and global
770 warming, in: *The Global Circulation of the Atmosphere*, Princeton University Press, 267–301, 2021.
771
772 Ngandam Mfondoum, A. H., Wokwenmendiam Nguet, P., Mefire Mfondoum, J. V., Tchindjang, M.,

773 Hakdaoui, S., Cooper, R., Gbetkom, P. G., Penaye, J., Bekoa, A., and Moudioh, C.: Adapting sudden
774 landslide identification product (SLIP) and detecting real-time increased precipitation (DRIP)
775 algorithms to map rainfall-triggered landslides in Western Cameroon highlands (Central-Africa),
776 *Geoenvironmental Disasters*, 8, <https://doi.org/10.1186/s40677-021-00189-9>, 2021.
777

778 Nicholson, S. E., Fink, A. H., Funk, C., Klotter, D. A., and Satheesh, A. R.: Meteorological causes of
779 the catastrophic rains of October/November 2019 in equatorial Africa, *Global. Planet. Change*, 208,
780 103687, <https://doi.org/10.1016/j.gloplacha.2021.103687>, 2022.
781

782 Oueslati, B., Yiou, P., and Jézéquel, A.: Revisiting the dynamic and thermodynamic processes
783 driving the record-breaking January 2014 precipitation in the southern UK, *Sci. Rep-Uk.*, 9,
784 <https://doi.org/10.1038/s41598-019-39306-y>, 2019.
785

786 Pokam, W. M., Djiotang, L. A. T., and Mkankam, F. K.: Atmospheric water vapor transport and
787 recycling in Equatorial Central Africa through NCEP/NCAR reanalysis data, *Clim. Dynam.*, 38,
788 1715–1729, <https://doi.org/10.1007/s00382-011-1242-7>, 2011.
789

790 Pokam, W. M., Bain, C. L., Chadwick, R. S., Graham, R., Sonwa, D. J., and Kamga, F. M. (2014):
791 Identification of processes driving low-level westerlies in West Equatorial Africa, *J. Climate*, 27,
792 4245–4262, <https://doi.org/10.1175/jcli-d-13-00490.1>.
793

794 Seager, R., Naik, N., and Vecchi, G. A.: Thermodynamic and dynamic mechanisms for large-scale
795 changes in the hydrological cycle in response to global warming*, *J. Climate*, 23, 4651–4668,
796 <https://doi.org/10.1175/2010jcli3655.1>, 2010.
797

798 Sheng, B., Wang, H., Li, H., Wu, K., and Li, Q.: Thermodynamic and dynamic effects of anomalous
799 dragon boat water over South China in 2022, *Weather and Climate Extremes*, 40, 100560,
800 <https://doi.org/10.1016/j.wace.2023.100560>, 2023.
801

802 Sonkoué, D., Monkam, D., Fotso-Nguemo, T. C., Yepdo, Z. D., and Vondou, D. A.: Evaluation and
803 projected changes in daily rainfall characteristics over Central Africa based on a multi-model
804 ensemble mean of CMIP5 simulations, *Theor. Appl. Climatol.*, 137, 2167–2186,
805 <https://doi.org/10.1007/s00704-018-2729-5>, 2018.
806

807 Taguela, T. N., Pokam, W. M., and Washington, R.: Rainfall in uncoupled and coupled versions of
808 the Met Office Unified Model over Central Africa: Investigation of processes during the September–
809 November rainy season, *Int. J. Climatol.*, 42, 6311–6331, <https://doi.org/10.1002/joc.7591>, 2022.
810

811 Tamoffo, A. T., Vondou, D. A., Pokam, W. M., Haensler, A., Yepdo, Z. D., Fotso-Nguemo, T. C.,
812 Tchotchou, L. A. D., and Nouayou, R.: Daily characteristics of Central African rainfall in the REMO
813 model, *Theor. Appl. Climatol.*, 137, 2351–2368, <https://doi.org/10.1007/s00704-018-2745-5>, 2019.
814

815 Tamoffo, A. T., Weber, T., Akinsanola, A. A., and Vondou, D. A.: Projected changes in extreme
816 rainfall and temperature events and possible implications for Cameroon’s socio-economic sectors,
817 *Meteorol. Appl.*, 30, <https://doi.org/10.1002/met.2119>, 2023b.
818

819 Tamoffo, A. T., Dosio, A., Weber, T., and Vondou, D. A.: Dynamic and Thermodynamic
820 Contributions to Late 21st Century Projected Rainfall Change in the Congo Basin: Impact of a
821 Regional Climate Model’s Formulation, *Atmosphere-Basel*, 14, 1808,
822 <https://doi.org/10.3390/atmos14121808>, 2023a.
823
824

825 Tamoffo, A. T., Weber, T., Cabos, W., Sein, D. V., Dosio, A., Rechid, D., Remedio, A. R., and
826 Jacob, D.: Mechanisms of Added Value of a Coupled Global Ocean-Regional Atmosphere Climate
827 Model Over Central Equatorial Africa, *J. Geophys Res-Atmos.*, 129,
828 <https://doi.org/10.1029/2023jd039385>, 2024.
829

830 Vallès-Casanova, I., Lee, S., Foltz, G. R., and Pelegrí, J. L.: On the Spatiotemporal Diversity of
831 Atlantic Niño and Associated Rainfall Variability Over West Africa and South America, *Geophys.*
832 *Res. Lett.*, 47, <https://doi.org/10.1029/2020gl087108>, 2020.
833

834 Wainwright, C. M., Finney, D. L., Kilavi, M., Black, E., and Marsham, J. H.: Extreme rainfall in East
835 Africa, October 2019–January 2020 and context under future climate change, *Weather*, 76, 26–31,
836 <https://doi.org/10.1002/wea.3824>, 2020.
837

838 Wang, L. and Li, T.: Effect of vertical moist static energy advection on MJO eastward propagation:
839 Sensitivity to analysis domain, *Clim. Dynam.*, 54, 2029–2039, [38 38](https://doi.org/10.1007/s00382-019-</p></div><div data-bbox=)

840 05101-8, 2020a.

841

842 Wang, T. and Li, T.: Diagnosing the column-integrated moist static energy budget associated with
843 the northward-propagating boreal summer intraseasonal oscillation, *Clim. Dynam.*, 54, 4711–4732,
844 <https://doi.org/10.1007/s00382-020-05249-8>, 2020b.

845

846 Wantim, M. N., Ughe, W. G., Kwah, D. C., Bah, T. C., Quinette, N., and Ayonghe, S. N.: Forensic
847 investigation of the Gouache landslide disaster, Western Region, Cameroon, *Journal of the*
848 *Cameroon Academy of Sciences*, 19, 223–240, <https://doi.org/10.4314/jcas.v19i3.3>, 2023.

849

850 Washington, R., James, R., Pearce, H., Pokam, W. M., and Moufouma-Okia, W.: Congo Basin
851 rainfall climatology: Can we believe the climate models?, *Philos. T. R. Soc. B.*, 368, 20120296,
852 <https://doi.org/10.1098/rstb.2012.0296>, 2013.

853

854 Wen, N., Liu, S., and Li, L. Z. X.: Diagnosing the dynamic and thermodynamic effects for the
855 exceptional 2020 summer rainy season in the Yangtze River Valley, *J. Meteorol. Res-Prc.*, 36, 26–
856 36, <https://doi.org/10.1007/s13351-022-1126-2>, 2022.

857

858 Yanai, M. and Tomita, T.: Seasonal and interannual variability of atmospheric heat sources and
859 moisture sinks as determined from NCEP–NCAR reanalysis, *J. Climate*, 11, 463–482,
860 [https://doi.org/10.1175/1520-0442\(1998\)011<0463:saivoa>2.0.co;2](https://doi.org/10.1175/1520-0442(1998)011<0463:saivoa>2.0.co;2), 1998.

861

862 Zhao, D., Zhang, L., and Zhou, T.: Detectable anthropogenic forcing on the long-term changes of
863 summer precipitation over the Tibetan Plateau, *Clim. Dynam.*, 59, 1939–1952,
864 <https://doi.org/10.1007/s00382-022-06189-1>, 2022.

865

866 Zhou, L., Tian, Y., Myneni, R. B., Ciais, P., Saatchi, S., Liu, Y. Y., Piao, S., Chen, H., Vermote, E.
867 F., Song, C., and Hwang, T.: Widespread decline of Congo rainforest greenness in the past decade,
868 *Nature*, 509, 86–90, <https://doi.org/10.1038/nature13265>, 2014.

869